

**MULTI-SCALE NATURE OF COMPOSITE MATERIALS:
THREE CASE STUDIES**

**by
KAAN BİLGE**

**Submitted to the Graduate School of Engineering and Natural Sciences
in partial fulfillment of
the requirements for the degree of
Master of Science**

**Sabanci University
June, 2012**

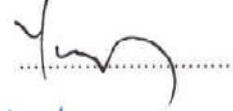
MULTI-SCALE NATURE OF COMPOSITE MATERIALS:
THREE CASE STUDIES

APPROVED BY:

Assoc. Prof. Dr. Melih Papila
(Thesis Advisor)



Prof. Dr. Yusuf Menciloglu



Prof. Dr. Ali Rana Atilgan



Assist. Prof. Dr. Mehmet Yıldız



Assoc. Prof. Dr. Nuri Ersoy



DATE OF APPROVAL:08/06/2012.....

© Kaan Bilge 2012
All Rights Reserved

Everything should be as simple as it is, but not simpler.

Albert Einstein

To my family

MULTI-SCALE NATURE OF COMPOSITE MATERIALS:
THREE CASE STUDIES

Kaan BILGE

MAT, Master of Science Thesis, 2012

Thesis Supervisor: Assoc. Prof. Dr. Melih Papila

Keywords: composite materials, hybrid composites, nanofiber, interlayer, micro-mechanics, textile composites, failure criteria

Abstract

Science and engineering of fiber reinforced advanced composite materials (FRC) is an actively broadening research field with more and more emphasis on their multi-phase and multi-scale characteristics. While emerging manufacturing and characterization techniques provide ability to manipulate the materials at all scales from traditional macro to relatively recent emergence of nano-scale, computational tools provide better understanding of behavior of composite materials. Collective and coherent use of these abilities and tools can make composites better. This thesis is an effort to address how and why engineers can and should associate other characteristic scales with the traditional macro-scale engineering of composites. Three different studies on structural composites which exemplifies the need for multi-scale overlook are reported, each contained in individual chapters.

Nano-Macro associated case study: In-house synthesized poly(styrene-co-glycidyl methacrylate) based nano-fibers manufactured by electro-spinning were implemented to carbon fiber reinforced epoxy composites as interlayers. As a result of several mechanical tests and fracture analysis a significant increase in resistance against mode II delamination (70%) and transverse matrix cracking (25%) with literally no weight

penalty was observed. This increase was attributed to the chemistry tuned epoxy compatibility of nano-fibrous interlayers.

Micro-Macro associated case study: A systematic statistical tool built upon an intensive amount of finite element analyses. Surrogate models on the micromechanics based stress amplification factors for CFRP reinforced epoxy composites are offered. Quadratic models are reported taking longitudinal fiber stiffness (E_f), fiber volume fraction (V_f) and matrix stiffness (E_m) as input and calculates each term of the stress amplification matrix that can connect macro-level stresses to micro-level stresses.

Meso-Macro associated case study: The fiber bundle width and inter-bundle distance of non-crimp fabric reinforcements (NCF) was considered. The effect of reinforcement architecture on the mechanical response was evaluated through the manufacturing and testing of vinyl ester based composite laminates containing glass fiber NCF of 300 TEX, 600 TEX, 1200 TEX and 2400 TEX yarn numbers with constant aerial weight. Overall results suggested that the inter-bundle distance was a tunable meso scale property that was effective especially under in-plane shear and longitudinal tensile loads.

KOMPOZİT MALZEMELERİN ÇOK BOYUTLU DOĞASI:
ÜÇ ÖRNEK DURUM ÇALIŞMASI

Kaan BILGE

MAT, Yüksek Lisans Tezi, 2012

Tez Danışmanı: Assoc. Prof. Dr. Melih Papila

Anahtar Kelimeler: kompozit malzemeler, hybrid kompozitler, nanolifler, mikromekanik, tekstil kompozitleri, kırılım kıstası

Özet

Elyaf takviyeli ileri kompozit malzemelerin incelenmesi ve tasarımı gün geçtikçe önem kazanan ve büyüyen bir araştırma alanıdır. Bu alanda güncel olarak üstünde durulan husus, bu malzemelerin çok fazlı ve çok boyutlu davranış özelliklerinin araştırılmasıdır. Gelişen üretim teknikleri ve karakterizasyon yöntemleri ile malzeme özellikleri, alışlagelmiş makro ölçekten başlayıp nano ölçeğe kadar incelenip, geliştirilirken diğer yandan hesaplamalı yöntemler kompozit malzemelerin farklı boyutlardaki davranışlarının araştırılmasına katkıda bulunmaktadır. Bu unsurların bir arada efektif kullanılması kompozit malzemelerin ilerlemesinde önemli bir etkidir.

Bu tez çalışması yapısal kompozit malzemeler üzerinde yapılan, üç örnek çalışmayı kapsamaktadır. Herbir çalışma sırasıyla nano, mikro ve mezo ölçeklerinde sınıflandırılabilen değişkenlerin, kompozit malzemelerin makro ölçekteki davranışına etkisini incelemektedir.

Nano-makro tabanlı örnek çalışmada, özgün sentezlenip elektrospin yöntemiyle üretilen Stiren glisidil metakrilat kopolimer bazlı nanolifler karbon elyaf destekli epoksi kompozitlerin içine katmanlar arası arafaz olarak yerleştirilmiştir. Bu eklemeni laminatların delaminasyon direncini %70 arttırırken aynı zamanda da yanal matris çatlamasını %25 geciktirdiği gözlemlenmiş ve nanoliflerin kimya bazlı epoksi uyumluluğu buna sebep olarak öne sürülmüştür.

Mikro-makro tabanlı örnek çalışmada, çok sayıda sonlu elemanlar analizini taban alan istatistiksel bir program geliştirilmiştir. Tepki yüzeyleri temelli yaklaşımları esas alan bu program karbon elyaf destekli epoksi kompozitler için fiber sertliği, hacimsel fiber oranı ve matris sertliği gibi parametreleri veri olarak alıp, makro ve mikro gerilimleri birbirine bağlayan mikromekanik bazlı gerilim yükseltme faktörlerini hesaplamaktadır.

Mezo-makro tabanlı örnek çalışma, kırimsız elyaf takviyeli kompozitler için mezo boyuttaki fiber demet enlerini ve demetler arasındaki uzaklığı değişken olarak almaktadır. Birim alan ağırlığı sabit, 300 TEX, 600 TEX, 1200 TEX ve 2400 TEX iplik numaralı cam elyaf kumaş destekli vinil ester kompozitlerin üretimi ve testiyle, bu değişkenlerin genel mekanik davranışa etkisi vurgulamaktadır.

Acknowledgments

As a profound prelude, I would like to express my special thanks and gratitude to Assoc. Prof. Dr. Melih Papila who has always been a source of guidance and inspiration for me with his continuous support and endless enthusiasm. Working with him not only gave me the opportunity to discover new horizons but taught me how to find them with a never ending patient and admiration. Besides, I sincerely thank to him for its personal support, both during my BSc and MSc studies.

I would also want to thank to my committee members Prof. Dr. Yusuf Mencelođlu, Prof. Dr. Ali Rana Atılgan, Assist.Prof. Dr. Mehmet Yıldız and Assoc. Prof. Nuri Ersoy. I am grateful for their willingness for both helping and supporting me in my research activities and for enriching my MSc thesis with their valuable comments and reviews.

I want to convey special acknowledgements to Ms. Gülnur Başer and Mr. Ergün Binbir from TELATEKS A.Ş and to Ms. Sila Suer and Dr. Ođuz Menekşe from ROKETSAN A.Ş for their fruitful collaboration.

I feel happy to thank to my dearest colleagues Elif Özden and Eren Şimşek both for their colorful ideas about my research and friendship. Furthermore, I owe a sincere thank to Mustafa Baysal, Ođuzhan Ođuz and Deniz Turgut with whom I have shared an important part of my life. And then there are all the other people who have made Sabanci University a very special place over two years: Firuze Okyay, Burcu Özel, Yeliz Ekinci, Melike Mercan Yıldızhan, Hasan Kurt, Erim Ülkümen, Ayça Abakay, Özge Malay, Hamidreza Khassaf, Özge Batu, Kinyas Aydın, Tuğçe Akkaş, Çınar Öncel, Fatih Fazlı Melemez, Talha Boz and all of the other people with whom I have shared the same enjoyable research environment.

Furthermore, I am thankful to TUBITAK for providing me scholarship and project funding (TUBITAK 109M651) during my thesis.

Finally, my deepest gratitude goes to my family for their love and support throughout my whole life.

TABLE OF CONTENTS

CHAPTER 1	1
1.1 General Introduction	1
CHAPTER 2 NANO-MACRO	3
2.1 Introduction	3
2.2 Experimental Procedure and Characterization	6
2.2.1 Copolymer Synthesis	6
2.2.2 Electrospinning Process and Laminate Manufacturing	7
2.2.3 Mechanical Testing	9
2.2.3.1 Three Point Bending Tests	9
2.2.3.2 End Notched Flexure (ENF) Test	10
2.2.3.3 Un-notched Transverse Charpy Impact Testing	10
2.2.3.4 Longitudinal and Transversal Tensile Tests	11
2.2.4 Surface and Cross Sectional Characterization	11
2.3 Results and Discussion	12
2.3.1 MWCNTs in P(St-co-GMA) Nanofibers.....	12
2.3.2 Epoxy Wettability and Structural Compatibility of P(St-co - GMA)/MWCNT interlayers	13
2.3.3 Flexural Performance by Three-Point Bending Tests	16
2.3.4 Mode II Strain Energy Release Rate by ENF tests	20
2.3.5 Un-notched Charpy Impact Test Results	23
2.3.6 Transversal Tension Test Results	23
2.3.7 Longitudinal Tensile Test Results	25
2.4 Conclusions	27
2.5 References	28

CHAPTER 3 MICRO-MACRO	31
3.1 Introduction	31
3.2 Methodology	33
3.2.1 Concept of “Experiment”.....	33
3.2.2 Planning and Analysis of Experiments:	
Response Surface Methodology	33
3.2.2.1 Design of Experiments	33
3.2.2.2 Determination of Parameter Ranges	34
3.2.2.3 Responses: Mechanical Stress Amplification Factors	37
3.2.2.4 Regression Analysis	39
3.3 Results and Discussion	40
3.3.1 Verification of FE Based Stress Analysis	40
3.3.2 Surrogate Models for Stress Amplifications on Fiber/Matrix Interfac (F1, F2, F3) and Matrix Phase (IF1, IF2, IS)	44
3.3.3 Surrogate Model Adequacy Checking and Parameter Effects	49
3.4 Conclusion and Future Works	52
3.5 References	54

CHAPTER 4 MESO-MACRO	59
4.1 Introduction.....	59
4.2 Experimental Procedure and Characterization	61
4.2.1 Materials	61
4.2.2 Laminate Manufacturing	62
4.2.3 Mechanical Testing	63
4.2.4 Loss on Ignition Methodology For Fiber Volume Fraction Determination	64
4.3 Results and Discussion	65
4.3.1 Fiber Volume Fraction of Laminates	65
4.3.2 Effect on Longitudinal and Transverse Tensile Strength of Composite Laminates	65
4.3.3 Effect on the In-Plane Shear Strength of Composite Laminates	68
4.3.4 Effect on the Longitudinal and Transversal Compressive Strength	69
4.3.5 Tsai-Wu Based Failure Envelopes and Correction Cases	71
4.3.6 Micromechanics Based Back-Calculation of Constituent Properties	74
4.4 Conclusion	78
4.5 References	80

LIST OF FIGURES

Figure 2.1: Schematic representation of poly(Styrene-co-glycidylmethacrylate) synthesis	6
Figure 2.2: Electro-spinning over the prepreg plies	7
Figure 2.3: Vacuum bagging and curing	8
Figure 2.4: Three- point bending test configurations and lamination sequences	9
Figure 2.5: ENF test configurations and lamination sequence	10
Figure 2.6: a) A single P(St-co-GMA)/MWCNT nanofiber b) MWCNTs on the surface of the nanofiber c) Walls of MWCNT	12
Figure 2.7: Nanofiber morphologies on the prepreg surfaces: a, b) at room temperature, c, d) at 100°C.	13
Figure 2.8: Nanofibrous mat over the prepreg layers a) Just after electro- spinning. b) 30 minutes after at 100°C c,d) Zoomed in view for fiber/epoxy interaction at 100°C	14
Figure 2.9: An epoxy/hardener drop on the P(St-co-GMA)/MWCNT surface	15
Figure 2.10: Representative three point bending test curves for (0) ₃ laminates	17
Figure 2.11: Cross-sectional view of fractured three point specimens a) (0/0/0) b) (90/0/90) and c, d) Corresponding fracture surfaces.....	18
Figure 2.12: Representative three point bending test curves for (90/0/90) ₃ laminates .	19
Figure 2.13: Representative ENF test curves for (0) ₄ laminates	21
Figure 2.14: Fracture surfaces of a) neat epoxy ply-to-ply interface b) P(St- Co GMA)/MWCNT interlayered interface. Zoomed in views for c) encircled area in 1.13b. Arrows: the distinguishable damage marks d) encircled area in 1.13c, arrows: two distinct failure regions (carbon fiber interface and through interlayer/epoxy complex). e) encircled area in 1.13d. Damage marks on interlayer/epoxy complex.	22
Figure 2.15: Cross-sectional view of a fractured transverse tensile UDtest specimen a) neat epoxy ply-to-ply interface and b) P(St-co-GMA)/MWCNT interlayered c) Zoomed in view of encircled area	24
Figure 2.16: Representative transversal tensile test curves	25
Figure 2.17: Representative longitudinal tensile test curves	26

Figure 3.1: A three level full factorial cubodial design in coded domain	34
Figure 3.2: Fiber modulus and strength values for different carbon filament products.	35
Figure 3.3: Elastic modulus values for different epoxy products.	36
Figure 3.4: Mechanical stress amplification factor matrix acting on macro stresses. ..	38
Figure 3.5: Square array fiber distribution and critical nodes.	38
Figure 3.6: RVEs subjected to unit strains a) 11 direction b) 22 direction c) 33 direction d) 13 direction e) 12 direction f) 23 direction.....	43
Figure 3.7: Actual vs. Prediction plot and F-Ratios for M_{11} on F1, F2, F3	49
Figure 3.8: Actual vs. Prediction plot and F-Ratios for M_{22} on F1	50
Figure 3.9: Actual vs. Prediction plot and F-Ratios for M_{44} on F1 and F2	51
Figure 3.10: Actual vs. Prediction plot and F-Ratios for M_{55} (M_{66}) on F3(F1)	51
Figure 4.1: a) 300 TEX NCGF Fabric b) 600 TEX NCGF Fabric c) 1200 TEX NCGF Fabric d) 2400 TEX NCGF Fabric	61
Figure 4.2: a, b, c) Flow front during the vacuum infusion process d) A view from the post-cured laminate ready for specimen cutting	62
Figure 4.3: a) Representative stress-strain curves for longitudinal tensile tests b) Ply splitting fracture of $(0)_8$ laminates	66
Figure 4.4: a) Representative stress-strain curves for transversal tensile tests b) Matrix cracking fracture of $(90)_8$ laminates	67
Figure 4.5: a) Representative stress-strain curves for $(+45/-45)_4s$ laminates b) Shear mode fracture	68
Figure 4.6: a) Fractured $(0)_8$ laminates b) Side-view of fractured $(0)_8$ laminates c) Force-displacement curve for a $(0)_8$ laminate	70
Figure 4.7: Tsai-Wu Failure envelopes for $(0/90)_{4s}$ and $(0/+45/-45/90)_s$ laminates with 300 TEX NCGF reinforcement	72
Figure 4.8: Tsai-Wu Failure envelopes for $(0/90)_{4s}$ and $(0/+45/-45/90)_s$ laminates with 600 TEX NCGF reinforcement	72
Figure 4.9: Tsai-Wu Failure envelopes for $(0/90)_{4s}$ and $(0/+45/-45/90)_s$ laminates with 1200 TEX NCGF reinforcement	73
Figure 4.10: Tsai-Wu Failure envelopes for $(0/90)_{4s}$ and $(0/+45/-45/90)_s$ laminates with 2400 TEX NCGF reinforcement	73

LIST OF TABLES

Table 2.1: Three-Point Bending Test Results	16
Table 2.2: ENF Test Results	20
Table 2.3: Transversal Charpy Impact Test Results	23
Table 2.4: Transversal and Longitudinal Tensile Test Results	26
Table 3.1: Carbon fiber material data	37
Table 3.2: Epoxy material data	37
Table 3.3: Ply properties for the example case studied ($V_f=0,7$)	40
Table 3.4: Comparison of strain amplification factors at different critical points.....	41
Table 3.5: Comparison of effective property predictions	41
Table 3.6: Non-zero Coefficients β_s determined by stepwise regression for M_σ matrix on critical point F1	45
Table 3.7: Non-zero Coefficients β_s determined by stepwise regression for M_σ matrix on critical point F2	46
Table 3.8: Non-zero Coefficients β_s determined by stepwise regression for M_σ matrix on critical point IF1	47
Table 3.9: Non-zero Coefficients β_s determined by stepwise regression for M_σ matrix on critical point IS	48
Table 4.1: Fabric properties for different yarn number	62
Table 4.2: Coding of the manufactured laminates according to their lamination sequences	63
Table 4.3: Fiber volume fractions of manufactured laminates	65
Table 4.4: Longitudinal and transversal tensile test results	67
Table 4.5: In-plane shear strength and modulus values.....	69
Table 4.6: Longitudinal and transversal compressive strength and modulus values.....	71
Table 4.7: Test Results for $(0/90)_{4s}$ and $(0/+45/-45/90)_s$ laminates and predicted Tsai-Wu failure strengths	74
Table 4.8: Constituent properties for micromechanical analysis	75
Table 4.9: MMF based stress amplification factors for matrix and fiber phases	75
Table 4.10: Back calculated fiber strengths for different micromechanical models	76
Table 4.11: Back calculated resin strengths for different micromechanical models	76

CHAPTER 1

1.1 General Introduction

Science and engineering of fiber reinforced advanced composite materials (FRC) is an actively broadening research field with more and more emphasis on their multi-phase and multi-scale characteristics. While emerging manufacturing and characterization techniques provide ability to manipulate the materials at all scales from traditional macro to relatively recent emergence of nano-scale, computational tools provide better understanding of behavior of composite materials. Collective and coherent use of these abilities and tools can make composites better. This thesis is an effort to address how and why engineers can and should associate other characteristic scales with the traditional macro-scale engineering of composites. Three different studies on structural composites which exemplifies the need for multi-scale overlook are reported, each contained in individual chapters.

Nano-Macro associated case study: Nano-scale considerations in structural composites field emerged from the fact that nano-scale reinforcements as distinct phase(s) are expected to elevate mechanical properties without significant weight penalty. While aiming to achieve improvements passing on notably to the macro-scale, the understanding of the transmittal mechanisms between nano and upper length scales requires multi-disciplinary experimental and analytical research efforts. In order to contribute to this wide open end, Chapter 2 investigates the use of in-house synthesized poly(styrene-co-glycidyl methacrylate) based nano-fibers manufactured by electro-spinning as interlayer agents to improve delamination and transverse matrix cracking resistance of carbon fiber reinforced epoxy composites. The effort also includes the effect of Multi Walled Carbon Nanotubes (MWCNTs) inside of the nanofibers to the overall behavior composite laminates. Overall an example of hybrid composites where nano-scale phases provide improvements at macro level properties are presented.

Micro-Macro associated case study: the micro-scale engineering of composite materials has become rather a conventional method that offers useful insight to the

macro scale observations. A substantial amount of research activity was directed towards the micromechanics of composite materials to provide more accurate representation of heterogeneous materials at macro-scale in homogenized manner. While stiffness aspects benefit from the homogenized scheme, recent failure prediction schemes are driven by constituent-based assessments via micromechanics models along with the macro and homogenized stresses. This is because traditional macro stress based failure criteria (e.g Tsai-Wu, Tsai-Hill, Max Stress, Max Strain) to predict the complex behavior of composite materials may remain limited. Based on the micromechanics of failure (MMF), third chapter presents a systematic statistical tool built upon an intensive amount of finite element analyses. Surrogate models on the micromechanics based stress amplification factors for CFRP reinforced epoxy composites are offered. Quadratic models are reported taking longitudinal fiber stiffness (E_f), fiber volume fraction (V_f) and matrix stiffness (E_m) as input and calculates each term of the stress amplification matrix that can connect macro-level stresses to micro-level stresses. These general user oriented surrogates enable the use of MMF without involved micromechanics based FE analysis.

Meso-Macro associated case study: Increased use of non-crimp fabric (NCF) in addition to traditional fabric composites backs-up extensive efforts to understand the behavior at the meso-scale. Need for the meso scale insight of such composites is due to complex tow-yarn architectures in contrast to uniformly spread traditional uni-directional tape reinforcements where typically micro-macro coupling is sufficient. The last chapter deals with the effect of yarn linear density or so called TEX number on the behavior of non-crimp glass fiber reinforced vinyl ester composites. Meso scale factors in NCF composites can be described as inter-bundle distance and fiber bundle width. Their effects to the overall mechanical response are investigated through the manufacturing and testing of composite laminates containing glass fiber NCF of 300 TEX, 600 TEX, 1200 TEX and 2400 TEX yarn numbers while aerial weight remained constant. Experiment based Tsai-Wu strength and stiffness parameters of several laminates are extracted out for macro-stress based property prediction with Tsai-Wu failure criteria. In addition, measured volume fractions and stiffness parameters were used in the micromechanical analysis for the strength back calculation of tested constituents. This part of the thesis exemplifies how meso-scale characteristics impact the experimental responses and shows the need of multi-scaled analysis (micro-meso-macro) in the explanation of such complex behavior.

CHAPTER 2

NANO-MACRO

STRUCTURAL COMPOSITES HYBRIDIZED WITH EPOXY COMPATIBLE POLYMER/MWCNT NANOFIBROUS INTERLAYERS

2.1 Introduction

Intra-and inter-laminar resistance to failure in laminated composite materials has been an active and constantly growing research field. Improvement in failure resistance is typically sought by i) altering the constituent properties, ii) introducing effective sub-phases and reinforcement without significant weight penalty including ply stitching and z-pinning applications.

Matrix toughening and interlayer toughening, for instance, have emerged to increase delamination resistance [1]. Reneker and co-workers [2] introduced an innovative idea and demonstrated the utility of electrospun nanofibers as potential bulk toughening elements. In line with Reneker's work, Dzenis [3, 4] explored the use of electrospun nanofibers as interlayer toughening elements within the traditional laminated composites. Dzenis observed that entangled nanofibers improve interlaminar fracture resistance much like the hooks and loops in Velcro and also play a part in crack deflection, nanofiber pull-out, plastic deformation, and crack bridging [4]. This pioneering idea was then applied to several composite systems and studied under various testing conditions [5-10] which were thoroughly reviewed and discussed by Zucchelli et.al [11].

Targeting improved toughness, several studies offered the use of carbon nanotubes as toughening elements to increase ply by ply sticking and delamination resistance [12,13]. While these studies have been paving the way to the integration of nanocomposites into traditional composites, research on their modeling aspects have also been intensified. Effective modeling strategies of various complexities can be used to understand the characteristics [14-16] and to explore the potential of the nano composites [17]. Review articles by Zeng et al. [14], Hu et al. [15] and more recently Llorca et al. [16] provide insight to the state-of-the-art on computational techniques, ranging from molecular dynamics simulations to traditional finite element analysis, to address the multi-scale nature of the nano-composite/composite world. It is our interpretation that integration of nano-composites, nanofibrous filler forms in particular, into conventional structural composites calls for both further data generation and multiscale modeling or framework for accurate mechanical/structural behavior predictions.

Our present work is intended to contribute the experimental demonstration and data generation of the nanofiber reinforced interlayers in laminated composites. In support of the effective use of electrospun nanofibers in structural composites, our previous efforts [18, 19] introduced the concept of tailoring or designing the chemistry of electrospun fiber and their interface with the polymer matrix. Our experiments revealed that polystyrene-co-glycidyl methacrylate P(St-co-GMA) is a promising base polymer for nanofiber production due to its chemical compatibility with the crosslinking epoxy systems in composite applications.

The content of this chapter aims to show the potential of electrospun P(St-co-GMA)/MWCNT based nanofibers as interlayers in conventional carbon fiber reinforced epoxy laminates. Since the choice of nanofiber chemistry points to the desirability of nanofiber-matrix compatibility and complete epoxy wettability, reinforcing abilities of the nanofibrous interlayers against transverse matrix cracking and delamination are explored. The overall experimental procedure beginning from the co-polymer synthesis and ending with the testing of composite laminates is explained in detail. Special attention is given to the characterization of nanofiber/matrix interaction at the laminate curing temperature. As for mechanical testing, the flexural performance increase through the incorporation of nanofibrous interlayers is reported through 3 point bending test results. Resistance against delamination is measured in mode II by end notched

flexure (ENF) tests whereas transverse matrix cracking resistance is primarily characterized by transverse Charpy impact tests and transversal tensile tests. The in-plane reinforcement ability is characterized by longitudinal tensile tests. The fracture modes and the fracture surfaces of the failed laminates are investigated to provide supporting information to the reinforcement effect.

As an overall view, the content of this chapter will be informative about the manufacturing of nanofibers through electrospinning, the in-situ interaction of P(St-co-GMA)/MWCNT nanofibers with epoxy systems and the advantages of using those materials in the conventional composite materials as interlayers to increase the resistance against matrix cracking and delamination.

2.2 Experimental Procedure and Characterization

2.2.1 Copolymer Synthesis

The monomers of styrene (purified) and glycidylmethacrylate (GMA) were supplied by Aldrich Chemical Co, whereas the solvents, *N,N* dimethylformamide and methanol, were purchased from Merck Chemicals Co. Copolymer poly(St-*co*-GMA) was synthesized by solution polymerization technique. Purified styrene and GMA (by weight fractions: $m=0.9$ styrene and $n=0.1$ GMA) (Figure 2.1) were mixed in a test tube contained in an ice bath. Dimethylformamide (DMF) was then added into St-GMA monomer mix such that volume proportion was 3:2, respectively. The initiator azobisisobutyronitrile (AIBN) was then added into the test tube flushed with nitrogen.

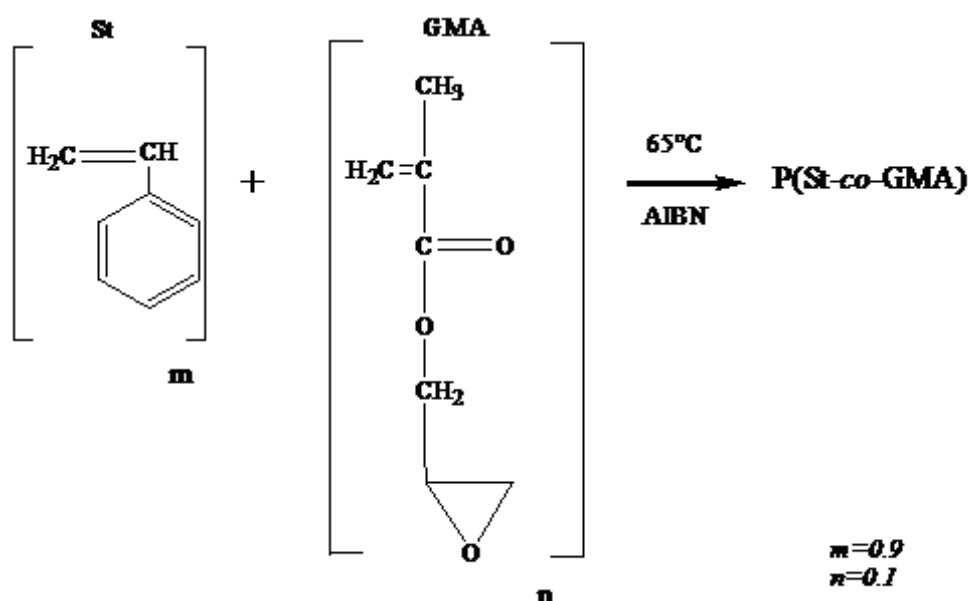


Figure 2.1: Schematic representation of poly(Styrene-*co*-glycidylmethacrylate) synthesis

The tube containing the dissolved monomers was then kept 24 h in the constant temperature bath at 65°C for the polymerization reaction. Finally, the polymer solution was poured out into a beaker containing methanol for precipitation.

Obtained methanol/polymer mixture was filtered and dried in an oven at 60 °C for 2 h. 30 wt.% P(St-co-GMA)/DMF polymer solutions were prepared and stirred magnetically for 3 hours to obtain homogeneity.

For MWCNT containing polymer solutions, 1 wt% of MWCNT was added to the same polymeric solution and the stirring time was set to 24 hours for the dispersion of MWCNTs inside of the polymeric solution.

2.2.2. Electro-spinning Process and Laminate Manufacturing

Polymeric nanofibers were obtained with electrospinning where an electrical bias potential (via Gamma High Voltage ES 30P-20W) of 15kV was applied to the polymer solutions contained in 2 mL syringe with a needle diameter of 300 μm (Figure 2.2) A syringe pump (NewEra NE-1000 Syringe Pump) was used to maintain a solution flow

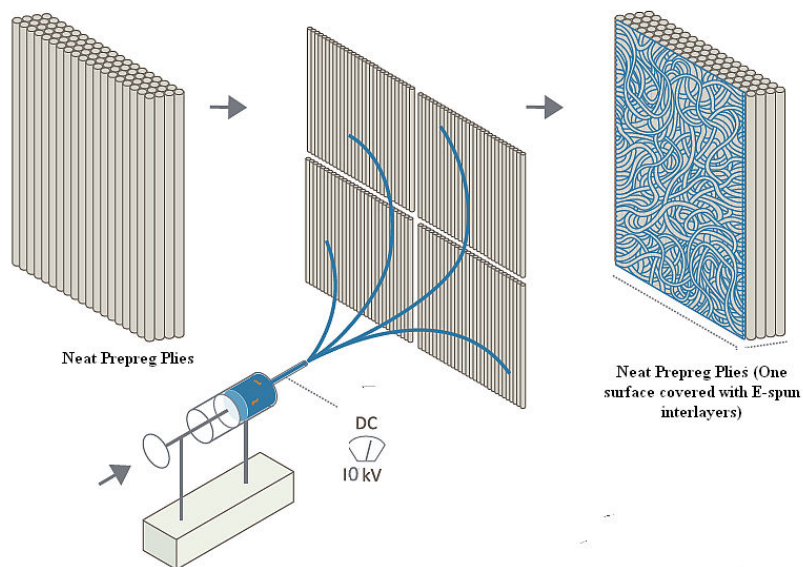


Figure 2.2: Electro-spinning over the prepreg plies

rate of 30 $\mu\text{L}/\text{h}$. Cut prepreg layers purchased from TCR Composite Ltd. containing Zoltek standard modulus PX-35-50K-11 carbon fibers embeded in UF3325-100 thermosetting epoxy with an average fiber volume fraction of 63%, were placed over

the grounded collector that was 10cm away from the syringe needle. The polymer solution was electrospun directly onto carbon/epoxy prepreg layers. Consequently, a thin homogenous layer of nanofibers, was electrospun on the prepreg surface forming the interlayer with an additional weight as low as 0.2% of the prepreg ply weight.

Note that whether being subject to electrospin or not, out-of-the freezer time and conditions of the prepreg plies were kept consistent throughout the study. After stacking the plies for intended laminates, each stack was put on a metallic tooling plate along with a release film and peel ply (Figure 2.3). Another sheet of peel ply was then laid on the pile of plies followed by a nonwoven breather layer. Next, the whole lay-up was vacuum bagged and kept under vacuum during the cure cycle. The cure temperature was primarily selected in accordance with the glass transition temperature of P(St-co-GMA) copolymer fibers [18] (T_g is around 100°C). Prepreg stacks were heated up to 100°C at a rate of $0.85^\circ\text{C}/\text{min}$, and hold time was 48 hours.

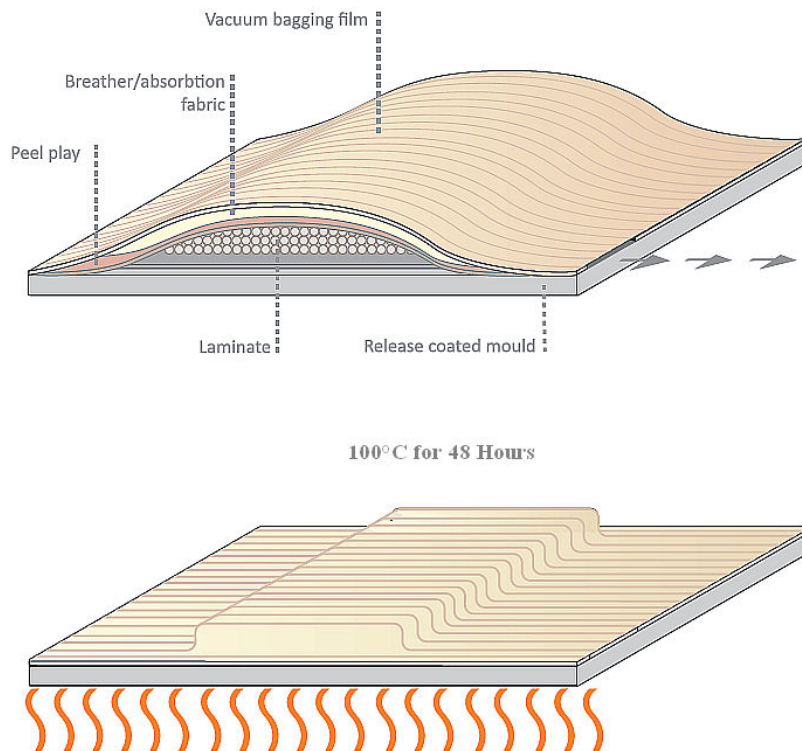


Figure 2.3: Vacuum Bagging and Curing

2.2.3. Mechanical Testing

Mechanical tests were performed using of Zwick Roell Z100 Universal Testing Machine and CEAST Resil Impactor machine. Loading rates and machine accessories were set up in accordance with the testing types namely, unnotched charpy impact, three point bending, end notched flexure and transversal tension tests.

2.2.3.1 Three Point Bending Tests

Flexural strength and modulus of interlayered and non-interlayered, (0/0/0) and (90/0/90) laminates were calculated via three point bending tests. For interlayered laminates, two interlayers on the interlaminar planes separated by a carbon/epoxy ply were added. Test configurations and preparation of the specimens were done according to ASTM D790 testing standards. Applied load versus crosshead displacement values were recorded and corresponding flexural strength (σ_f) and flexural modulus (E_B) values were calculated as follows:

$$\sigma_f = PL/2bd^2 E_B = L^3 m / 4bd^3$$

where P is the maximum load , m is the slope of the tangent to the initial straight-line portion of the load-displacement curve and b, d, L are specimen width, thickness and span length respectively.

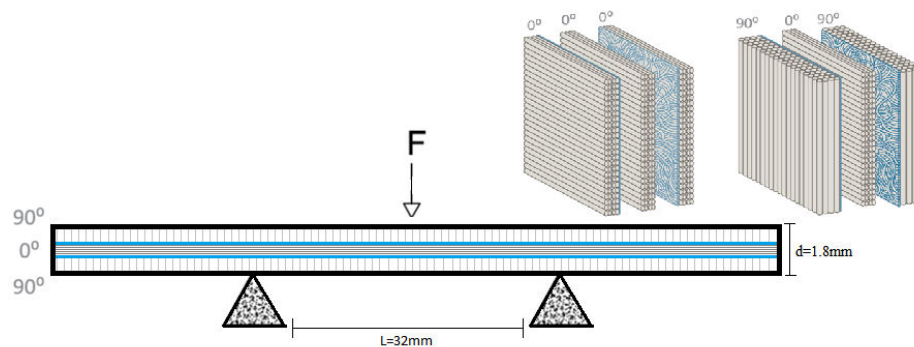


Figure 2.4: Three- point bending test configurations and lamination sequences

2.2.3.2 End Notched Flexure (ENF) Test

Mode II critical strain energy release rate (G_{IIc}) of the composite laminates was investigated by ENF tests. $(0)_4$ uni-directional laminates containing mid-surface delamination were tested under three point bending load configuration. A non-adherent, $30\mu\text{m}$ thick film layer was inserted to create the initial delamination during

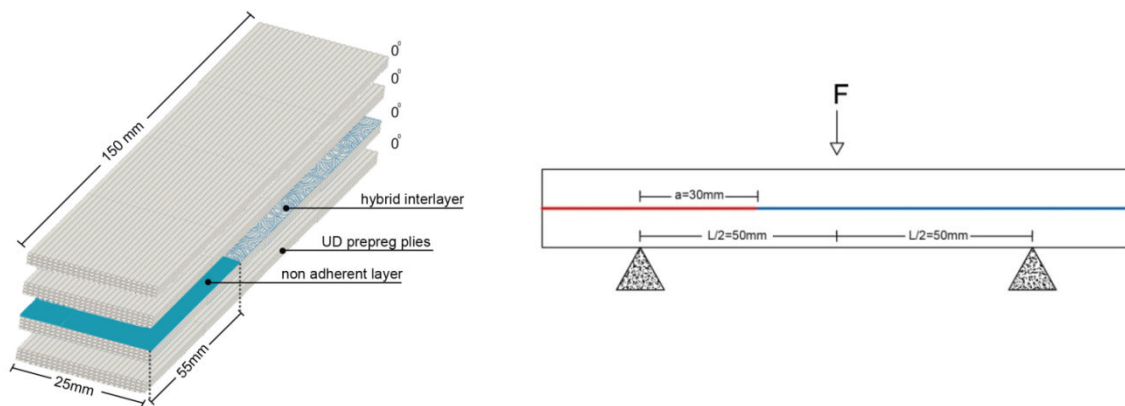


Figure 2.5: ENF test configurations and lamination sequence

consolidation of the laminates. Unlike the 3-pointbending tests the interlayer was inserted only at the midplane. Tests were conducted with a constant displacement rate of $1\text{mm}/\text{min}$ and G_{IIc} values were calculated using direct beam theory [20].

2.2.3.3 Un-notched Transverse Charpy Impact Testing

Charpy impact tests were performed in accordance with the ASTM D 6110 testing standards. Specimens of $(0)_4$ laminates were subjected to transversal impact loading from the longitudinal edge. Interlayered specimens contained 3 layers of interply reinforcement. An impact hammer of 4 Joule energy capacity was used with an initial release angle of 150° . Amount of energy absorbed upon transverse impact was recorded.

2.2.3.4 Longitudinal and Transversal Tensile Tests

Transverse and longitudinal tensile tests were performed in accordance with ASTM D3039 test standards. Laminates stacked as $(0)_4$ and $(90)_4$ having interlayers between the adjacent plies were tested. Tests were conducted with a constant displacement rate of 1mm/min. Maximum stress at failure was measured to determine the tensile strength of the tested laminates.

2.2.4 Surface and Cross Sectional Characterization

Cross section and fracture surface analysis of the composite laminates were carried out with a LEO Supra VP35 field emission scanning electron microscope after sputter deposition of a thin conductive carbon coating onto the samples. Distribution of MWCNTs in the nanofibers was investigated with a JEOL 2100 high resolution transmission electron microscope. Contact angle measurements of the epoxy resin on the electrospun fiber mats were performed using Kruss GmbH DSA 10Mk2 goniometer using DSA 1.8 software. 5mg droplets of resin/hardener mixture were put on the electrospun P(St-co-GMA) fibrous mat surface to investigate the epoxy wetting.

2.3 Results and Discussion

2.3.1 MWCNTs in P(St-co-GMA) Nanofibers

A systematic study on the electrospinning of P(St-co-GMA)/MWCNT fibers was carried out and reported by Ozden et. al [21]. We implemented the process parameters and material proportions suggested for successful introduction of the MWCNTs and the morphology of the fibrous webs [21]..

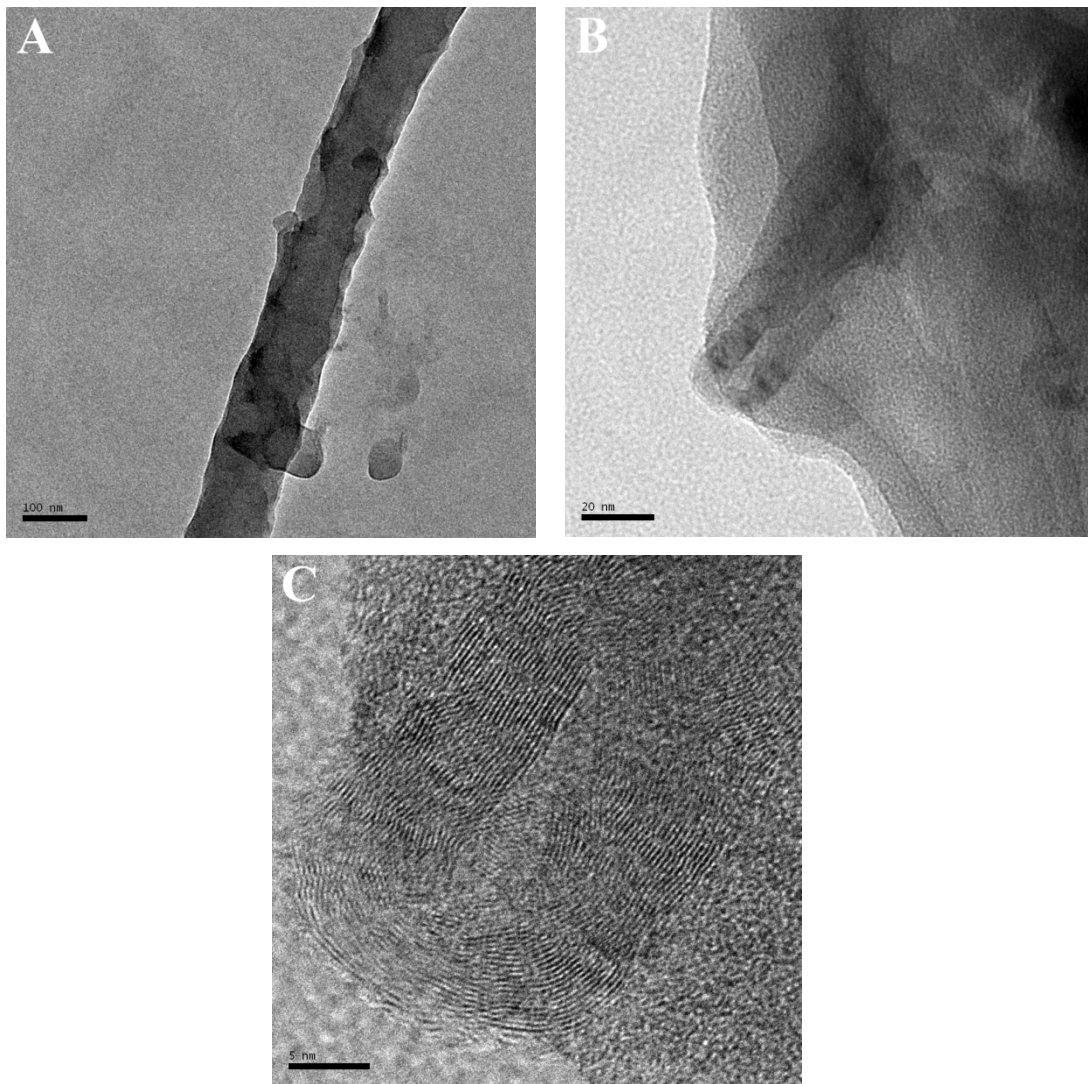


Figure 2.6: a) A single P(St-co-GMA)/MWCNT nanofiber c) A MWCNT on the surface of tthe nanofiber c) Walls of MWCNT

Figure 2.6 presents the TEM analysis of P(St-co-GMA) electrospun nanofibers composed of 1 wt% MWCNTs and demonstrates that MWCNTs were efficiently placed in the polymeric nanofibers as supplementary pin-like reinforcing elements

2.3.2 Epoxy Wettability and Structural Compatibility of P(St-co-GMA)/MWCNT interlayers

Figure 2.7a and 2.7b show the SEM images of P(St-co-GMA)/MWCNTs Nanofibers electrospun onto the prepreg surfaces at room temperature. Average fiber diameter ranged from 300 to 600nm. When the electrospun mat was heated up to 100°C, the non-woven fibrous morphology was transformed into a net-like structure composed of fibers connected at micron scale bead-like nodal points

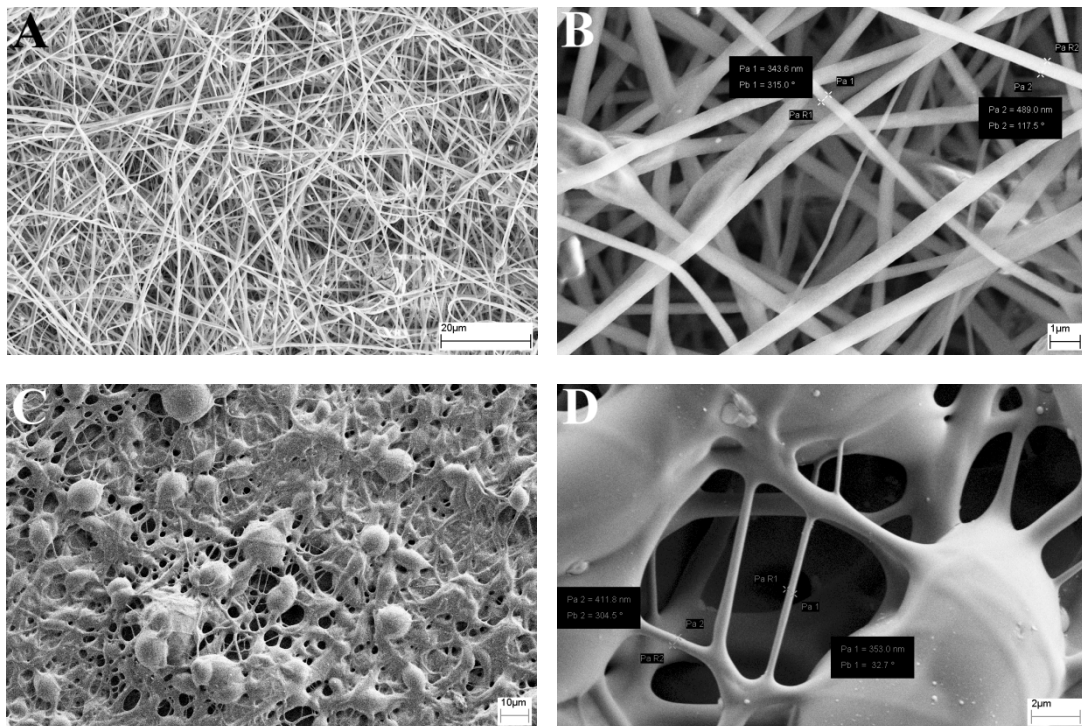


Figure 2.7: Nanofiber morphologies on the prepreg surfaces: a, b) at room temperature, c,d) at 100°C.

(Figure 2.7c and 2.7d). This change in the microstructure suggests the presence of a good interaction between fibrous interlayers and matrix phase at the laminate

curing temperature. This interaction was also observable macroscopically. Figure 2.8a-b show photographs of the electrospun layer-prepreg system kept at curing temperature 100°C (left hand side) and pristine samples at room temperature (right hand side) for comparison. It was quite visible that when the prepreg with the electrospun fibrous layer coat was heated, the epoxy matrix penetrated into the fibrous layer and wetting of the layer was completed even standing free with no vacuum bagging pressure (Figure 2.8b). Recall that the zoomed-in view of the surface of unheated laminate on Figure 2.8b appeared as shown in Figure 2.7a. However, when the temperature was increased, those layers of the majority of the nanofibers were no longer visible due to progressive self-wetting (Figure 2.8c and 2.8d).

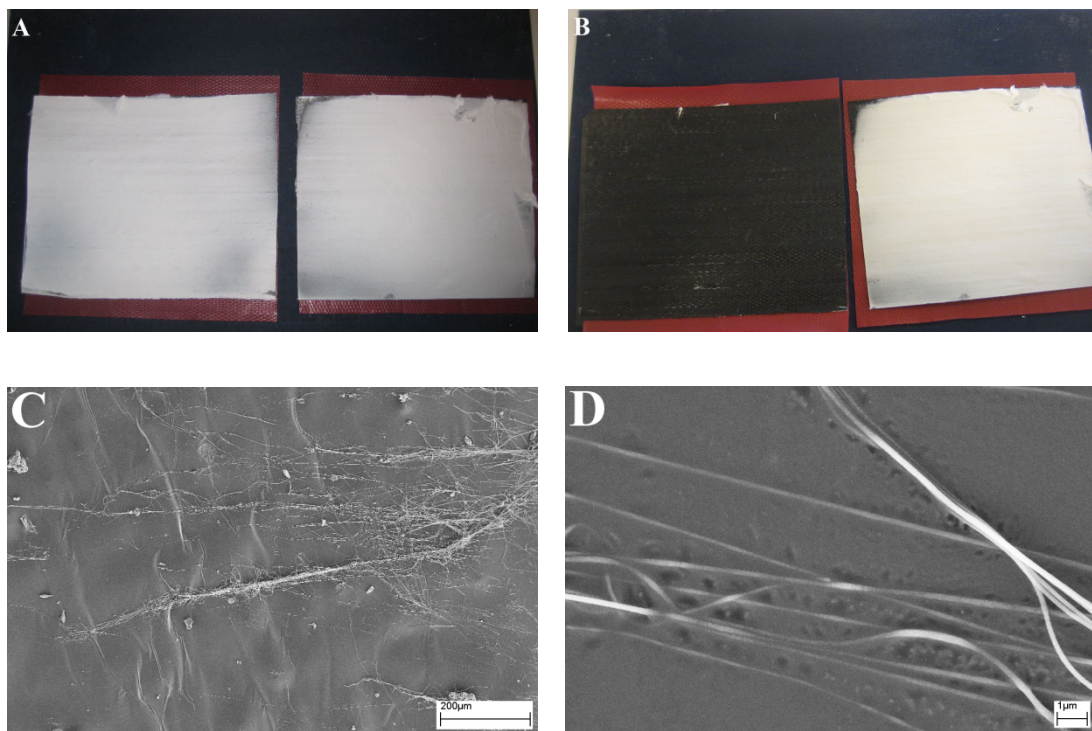


Figure 2.8: Nanofibrous mat over the prepreg layers a) Just after electrospinning. b) 30 minutes after at 100°C c,d) Zoomed in view for fiber/epoxy interaction at 100°C

Recall that the resin system was already at the stage B of curing upon purchasing meaning that there was no interaction between resin and the hardener. Parallel with the common knowledge, our macroscopic investigations suggested

that a substantial drop in the viscosity have occurred during resin dwell time. This drop allowed overall system to soften and to interact more efficiently with the nano-fibrous reinforcements. It was during that time interval that the interaction between resin and interlayers was maximized and the transition between figure 2.8a and 2.8b was hapenning.

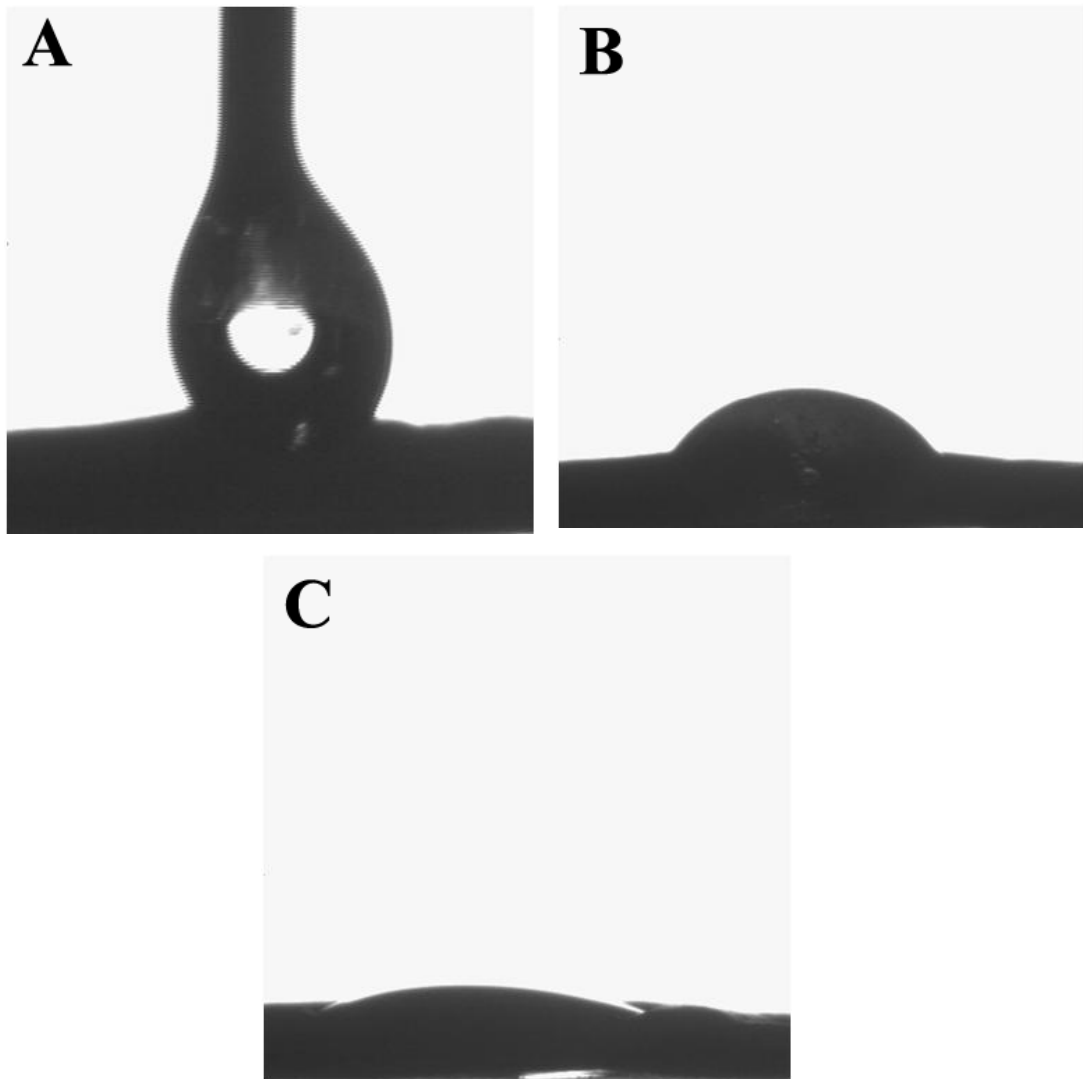


Figure 2.9: An epoxy/hardener drop on the P(St-co GMA)/MWCNT surface

More formal investigation of the wettability was performed via contact angle measurements with epoxy/hardener mixture on the surface of the electrospun mat.

When a droplet of epoxy/hardener mixture was put on the electrospun mat, it advanced and wetted the surface by leaving an average contact angle as low as $26.5^\circ \pm 6.1^\circ$, as shown in Figure 2.9. This result indicated that the viscous epoxy/hardener mixture could penetrate through the micropores in the fibrous surface morphology without challenging a remarkable capillary pressure due to the attractive forces [22], which is another indication of the chemical compatibility between the copolymer and the epoxy system.

2.3.3. Flexural Performance by Three-Point Bending Tests

Comparison of three point bending tests on laminates with and without fibrous interlayers showed that their addition led to increase in both flexural strength and modulus of the samples. The nanofibrous interlayers within the (0/0/0) laminates resulted in 11% and 17% increase in the flexural strength (σ_{flex}) and flexural modulus (E_{flex}), respectively (Table 2.1) Introduction of nanotubes by 1% weight to the copolymer fibers led to a further improvement adding up to 16% and 25% increase in the corresponding values compared to results without nanocomposite interlayers incorporated. Comparing (90/0/90) versus (90/I/0/I/90) laminates, P(St-co-GMA) nanofibrous interlayers increased both the flexural strength and modulus of the samples by 17%. The increase in these values were 21% and 29% with P(St-co-GMA)/MWCNT interlayers.

Table 2.1: Three-Point Bending Test Results

Specimen Type	Flexural Strength (MPa)	Flexural Modulus (GPa)
(0) ₃ Neat Laminates	875 ± 15.5	45.68 ± 0.8
(0) ₃ +P(St-co-GMA) Interlayer	965 ± 16.8	53,51 ± 0.8
(0) ₃ + P(St-co-GMA)/MWCNT Interlayer	1002 ± 14.2	57,3 ± 0.4
(90/0/90) Neat Laminates	242 ± 5.9	4.9 ± 0.2
(90/0/90) + P(St-co-GMA) Interlayer	283 ± 10.8	6,03 ± 0.6
(90/0/90) + P(St-co-GMA)/MWCNT Interlayer	296 ± 6	6,43 ± 0.9

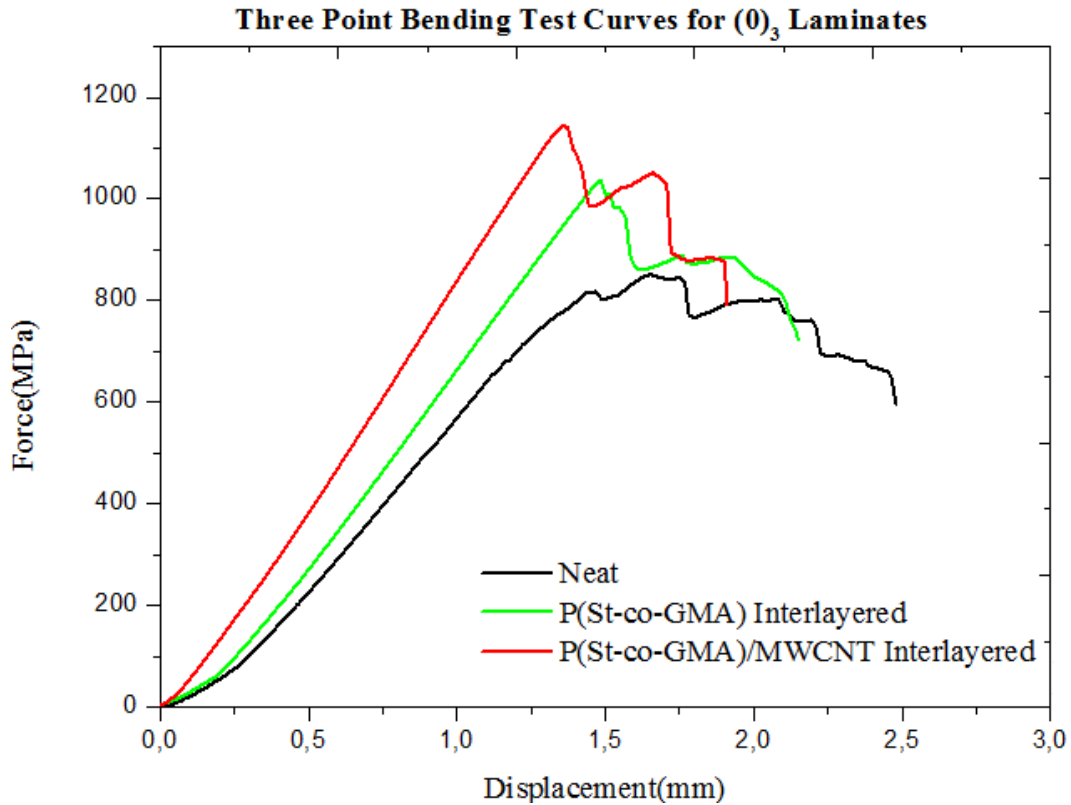


Figure 2.10: Representative three point bending test curves for $(0)_3$ laminates

Both stress-strain curves (figure 2.10) and post-failure SEM analyses on cross section of the specimens revealed that the lamination sequence was a factor in the fracture mode. Two distinct active failure mechanisms, transverse matrix cracking and/or delamination, were observed in $(0/0/0)$ laminates. Co-existence of the two failure mechanisms on the samples is attributed to the inability of the three point bending test to create pure shear conditions. An example is shown in the SEM image of a $(0/0)$ interface represented in Figure 2.11a where the two corresponding mechanisms were indicated with arrows (1: transverse matrix cracking and 2: delamination). Oblique intra-ply damage initiated at the end of delamination growth occurred due to the presence of high stress regions at the contact of the loading tip. The flexural strength and modulus increase reported by the three-point bending tests characterized both delamination resistance and matrix toughening introduced by the addition of the interlayer. This double effect

of the interlayer was also studied and introduced by Sihn et.al [5].

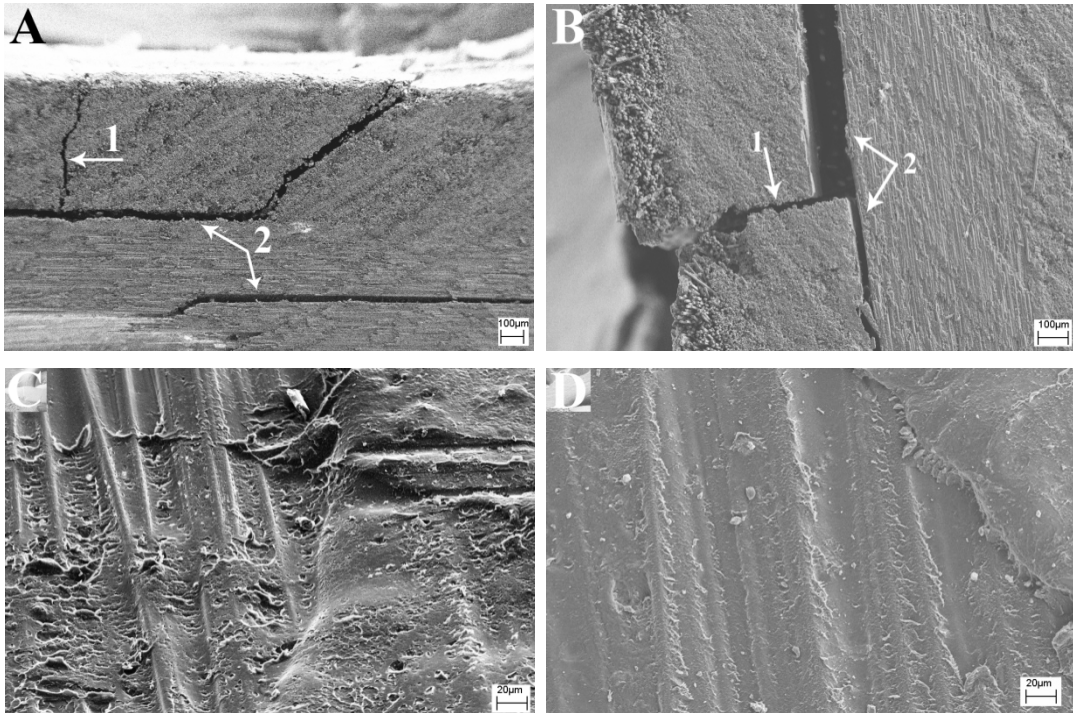


Figure 2.11: Cross-sectional view of fractured three point specimens
a) (0/0/0) b) (90/0/90) and c, d) Corresponding fracture
surfaces

With (90/0/90) lamination sequence, fracture mechanism was driven by 90° plies. The presence of 90° plies at the outer surface ensured the arising of interlaminar stresses at 90/0 interface due to the stiffness mismatch. In addition the inherent weak links of 90° plies to tensile loads triggered a matrix crack induced failure on the bottom ply during bending loading (Figure2.11b). Figure2.12 shows the representative flexural force-displacement curves of specimens with and without nanocomposite interlayers. The initial load drop (encircled in Figure 2.12) corresponds to the first ply failure due to the critical matrix cracking on the bottom 90° ply subjected to tension.

Note that the local matrix failure did not cause the ultimate failure. Instead a stable crack growth characterized by the load drops in Figure 2.12 was observed and the final fracture occurred when 90(failed)/0 interface progressed to delamination. Hence the overall flexural performance was governed by two major failure mechanisms. The increased resistance against initial matrix cracking may be noted by comparing the first ply failure loads whereas the delamination resistance of laminates may be compared by the ultimate load values. It is clearly visible from Figure 2.12 that the interlayer addition worked well for both mechanisms as it was suggested for (0/0/0) laminates.

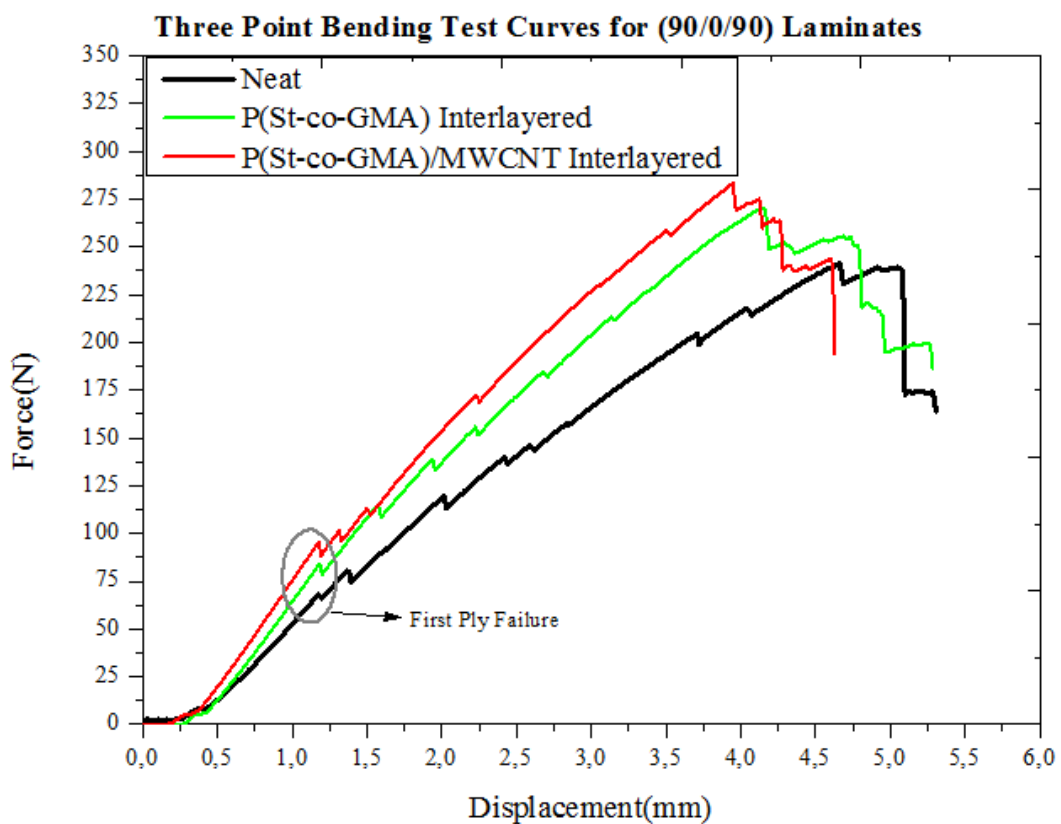


Figure 2.12: Representative three point bending test curves for (90/0/90) laminates

2.3.4. Mode II Strain Energy Release Rate by ENF tests

P(St-co-GMA) interlayer presence at the pre-crack tip increased G_{IIc} by 55 %. Further increase up to 70% in G_{IIc} by P(St-co- GMA)/MWCNTs interlayers suggests that the toughening is also correlated with the incorporation of the MWCNTs on electrospun fiber surfaces (Table 2.2).

Table2.2: ENF Test Results

Specimen Type	$G_{IIc}(\text{kJ/m}^2)$
$(0)_4$ Neat Laminates	0.95 ± 0.03
$(0)_4$ +P(St-co-GMA) Interlayer	1.47 ± 0.04
$(0)_4$ +P(St-co-GMA)/MWCNT Interlayer	1.6 ± 0.07

Failure of ENF specimens was observed as dominated by unstable crack growth parallel to the interlaminar plane with a sudden load drop. Formation of an unstable crack growth can be considered as an inherent characteristic in the testing of UD laminates under ENF test configurations with constant displacement rate [23]. Further analysis of the fracture surfaces also suggested that the increase observed in G_{IIc} was directly associated with the active role of interlayers on the fracture resistance. Common hackle patterns typically due to the micro-crack coalescence [24] all along the crack pathway are clearly visible on specimens without nanocomposite interlayers (Figure 2.14a). Whereas the hackle patterns for the interlayered specimens were either locally altered and replaced by a more complex structure or enlarged in size (Figure 2.14b).

A different fracture mode was noted as the capillary-like damage marks

indicated in Figure 2.14c. These damage marks were observed both in the areas consisting of epoxy-interlayer complex (left and right arrows) and around carbon fibers (center arrow) that is surrounded by epoxy-interlayer complex (Figure 2.14d). Close examination of the fracture pattern seen in Figure 2.14d revealed the presence of micro-crack formation through the interlayer-epoxy complex. This observation can be further supported by the cut-like damage marks inside of the interlayer-epoxy complex for which a zoomed-in image is shown in Figure 2.14e. Furthermore, the epoxy matrix and interlayers were not separated with a distinct interface, which was consistent with the structure shown in Figure 2.8c (image taken on ply).

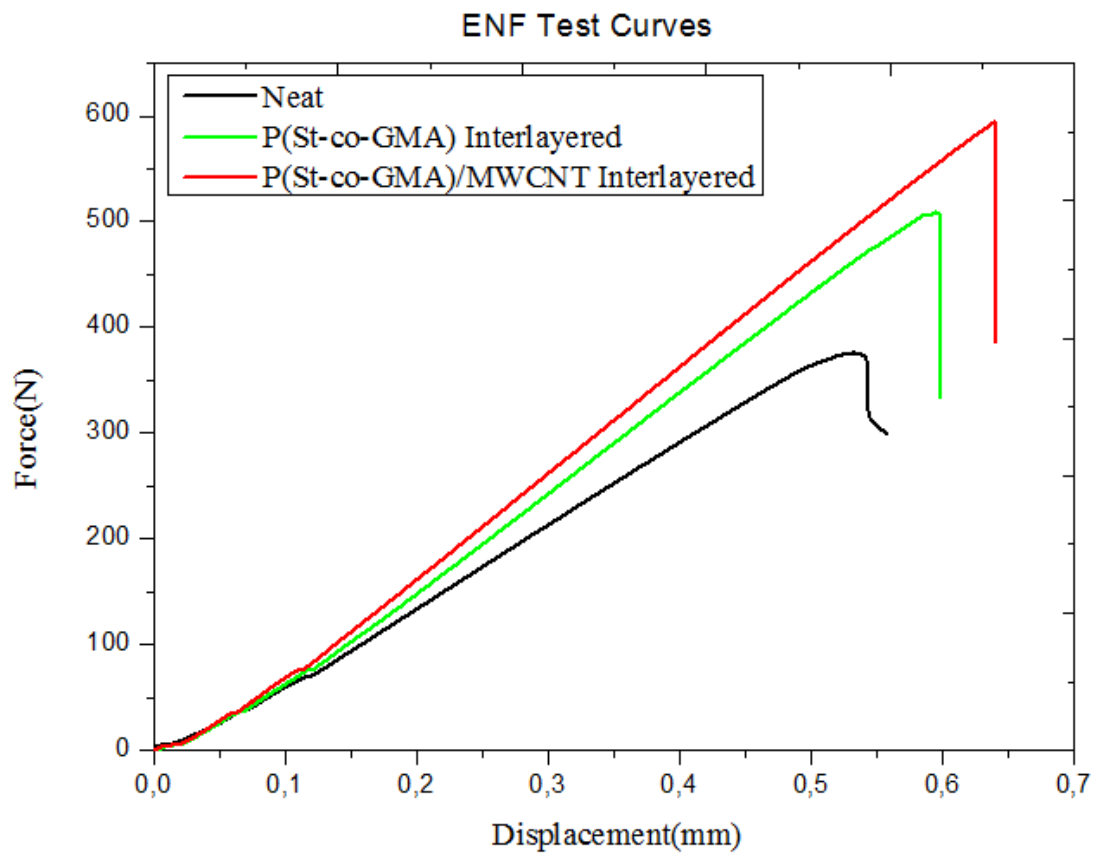


Figure 2.13: Representative ENF test curves for $(0)_4$ laminates

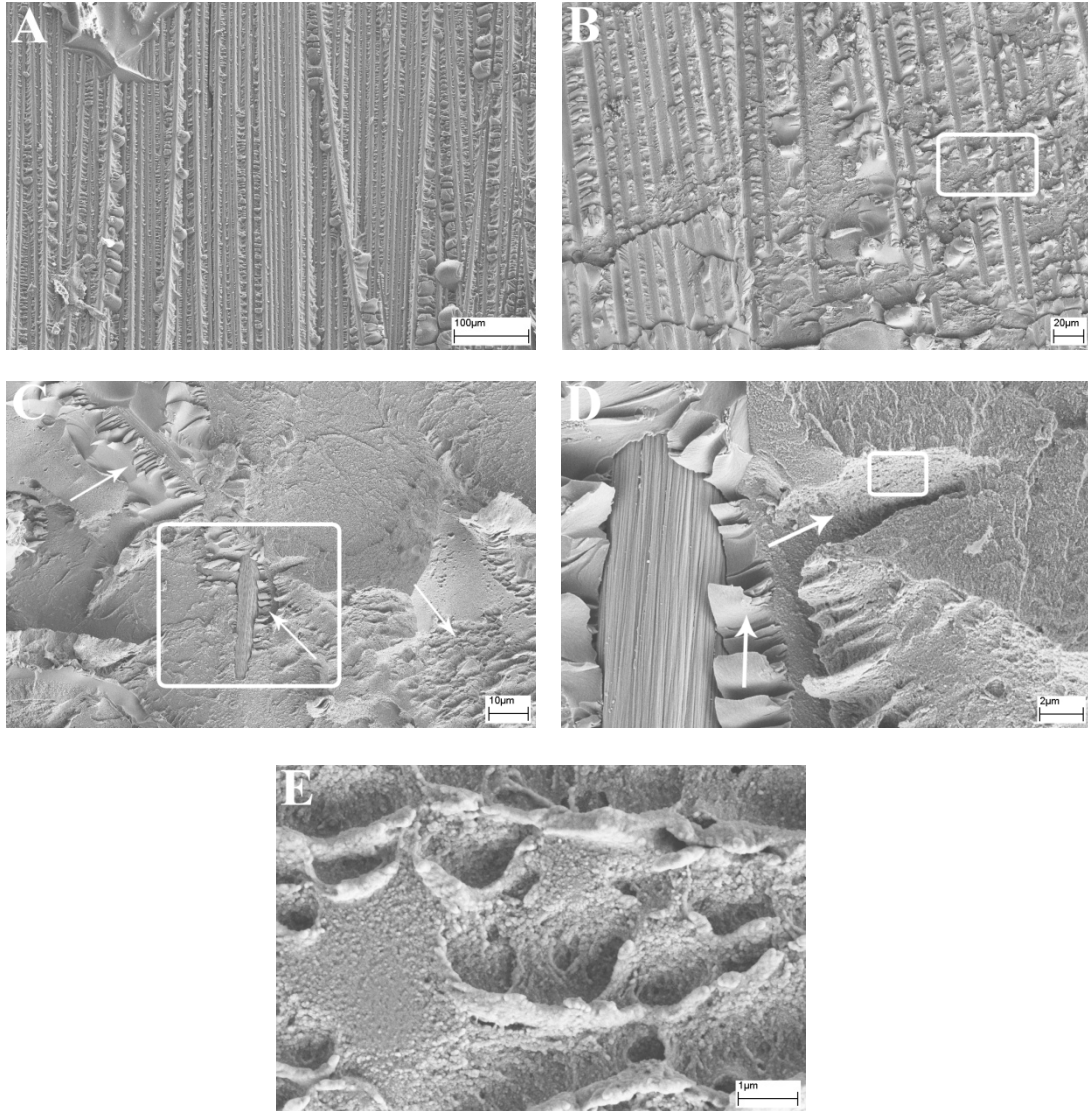


Figure 2.14: Fracture surfaces of a) neat epoxy ply-to-ply interface b) P(St- Co-GMA)/MWCNT interlayered interface. Zoomed in views for c)encircled area in 2.14b. Arrows: the distinguishable damage marks d) encircled area in 2.14c, arrows: two distinct failure regions (carbon fiber interface and through interlayer/epoxy complex). e) encircled area in 2.14d. Damage marks on interlayer/epoxy complex.

2.3.5. Un-notched Charpy Impact Test Results

The effect of interlayers against the transverse micro cracking as reported by preliminary three point bending results were further explored by Charpy impact tests. Unidirectional composite specimens were subjected to transversal impact (impact head to hit against the specimen longitudinal side wall rather than its surface) in order to create a failure initiated by sudden matrix cracking. An average increase up to 20% was recorded with the interlayered specimens. Moreover, in consistence with the results reported in previous sections, the presence of MWCNT on the fiber surfaces played a similar role in the overall performance of the laminates under impact loading conditions (Table 2.3).

Table 2.3: Transversal Charpy Impact Test Results

Specimen Type	Impact Energy Absorbed (kJ)
(0) ₄ Neat Laminates	1.72 ± 0.05
(0) ₄ +P(St-co-GMA) Interlayer	1.86±0.1
(0) ₄ +P(St-co-GMA)/MWCNT Interlayer	2.13±0.2

2.3.6. Transversal Tension Test Results

Transverse tensile tests of the uni-directional laminates offer an easy way to test for the effect of interlayers on the matrix dominated characteristics. Integration of P(St-co-GMA) and P(St-co-GMA)/MWCNTs interlayers on each ply resulted in 17% and 27% increase, respectively in transverse tensile strength (Table 1.3), with no weight penalty. These results correlate well with the previous Charpy impact tests where toughening by nanocomposite interlayers was associated with the increase in absorbed impact energy. Ultimate fracture of the UD transverse tension specimens was in the matrix cracking mode as expected (Figure 2.16). The cross sectional analysis of failed specimens further revealed the difference in ply-

to-ply resin structure at the interlaminar plane which was differentiated by the space between two subsequent carbon fibers as indicated in Figure 2.15a.

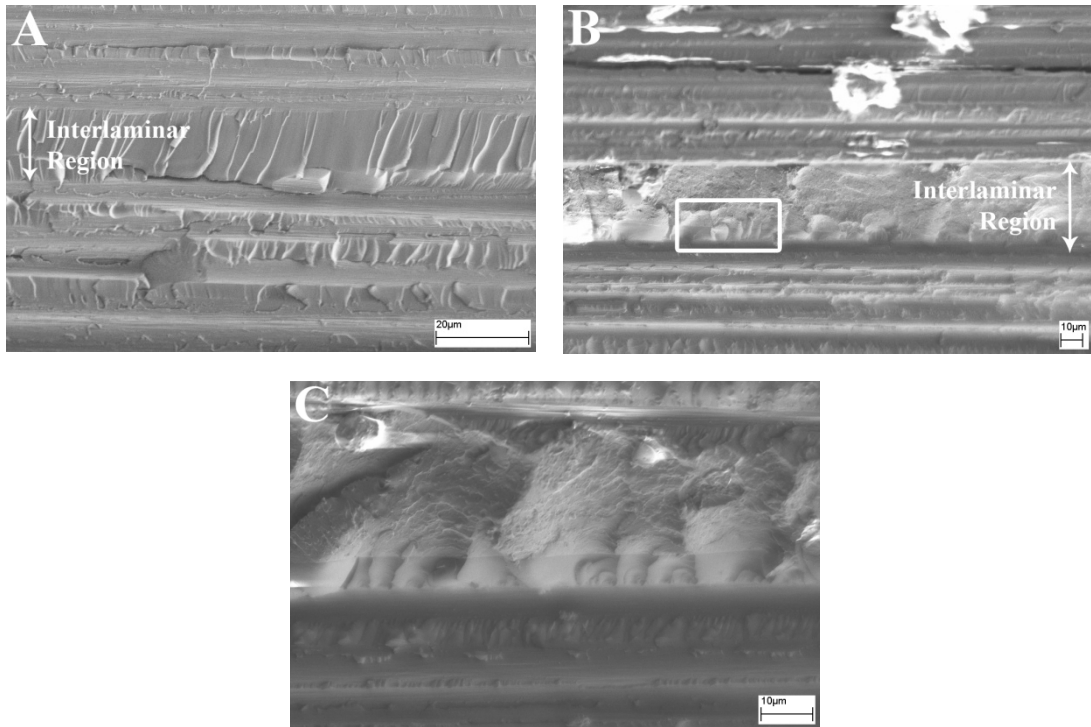


Figure 2.15: Cross-sectional view of a fractured transverse tensile UD test specimen a) neat epoxy ply-to-ply interface and b) P(St-co-GMA)/MWCNT interlayered c) Zoomed in view of encircled area in 8.

Figure 2.15a corresponds to the cross-sectional view of a laminate of neat epoxy interlayer where the damage marks occurred due to the resin fracture are clearly visible and the between-ply and in-ply resin fracture patterns are consistent. On the contrary, the resin morphology between the plies (ply-to-ply interface) and inside the plies were different on the cross-sectional fracture surface of the P(St-co-GMA)/MWCNTs interlayered specimens, as can be seen in Figure 2.15b.

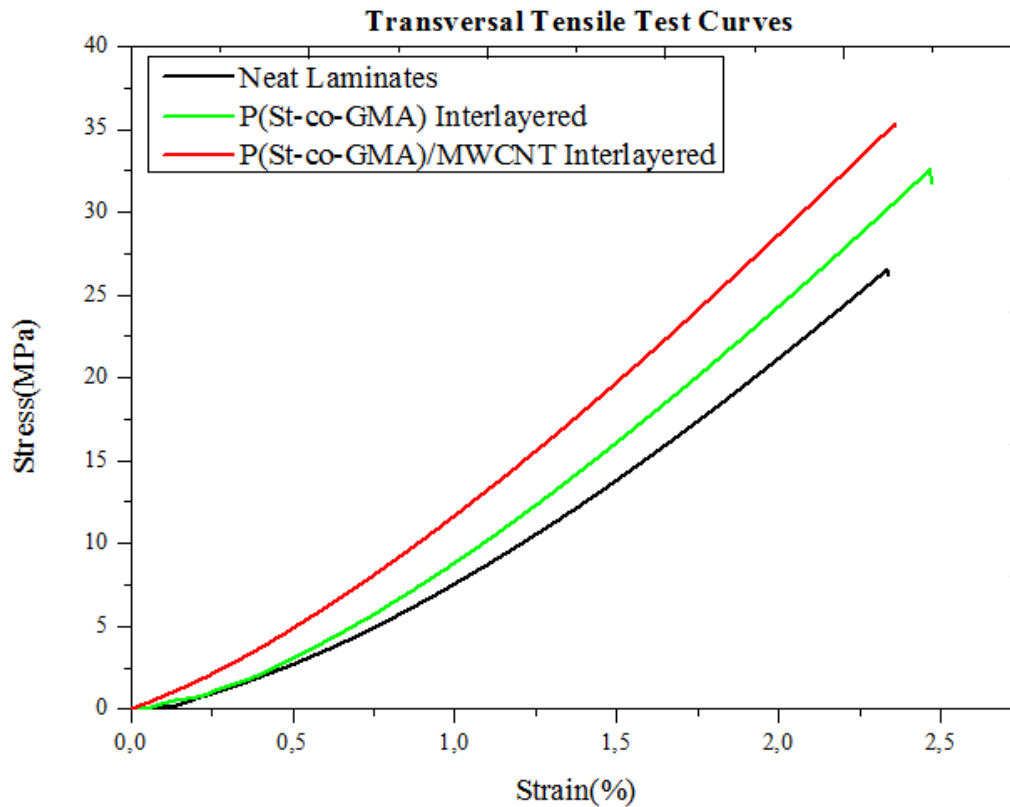


Figure 2.16: Representative transversal tensile test curves

2.3.7 Longitudinal Tensile Test Results

The contribution of nano-fibrous interlayer addition to the ultimate strength of the composite laminates was measured through longitudinal tensile tests of UD specimens. For this case, the addition of MWCNT was not considered. However, the presence of P(St-co-GMA) nanofibers on the interlaminar planes increased the ultimate tensile strength of the laminates up to 20 % which was indeed an important results. The ultimate fracture of test specimens has occurred due to ply splitting which was due to early critical matrix cracking causing the early failure. In that sense it is quite visible that the nano-fiber addition also increases the matrix toughness hence resisting more against transversal matrix cracks occurring under uni-axial tension loads. Along with transversal tensile strength the ultimate tensile strength results may be found in table 2.4.

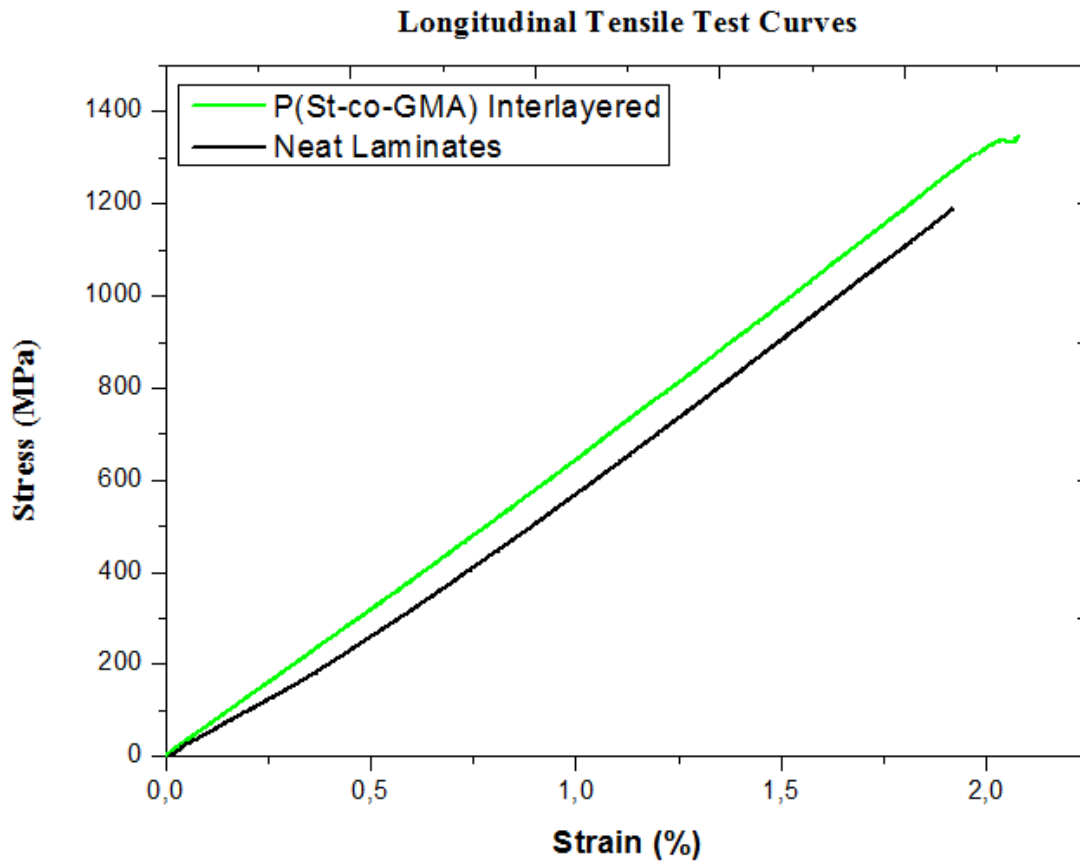


Figure 2.17: Representative longitudinal tensile test curves

Table 2.4: Transversal and Longitudinal Tensile Test Results

Specimen Type	Transversal Tensile Strength (MPa)	Ultimate Tensile Strength (MPa)
(0) ₄ Neat Laminates	26 ± 0.7	1090±25
(0) ₄ +P(St-co-GMA) Interlayer	31.2 ± 0.6	1298±35
(0) ₄ +P(St-co-GMA)/MWCNT Interlayer	34.6 ± 0.7	-

2.4 Conclusion

Electrospinning process was used to obtain nanofibrous P(St-co-GMA) and P(St-co-GMA)/MWCNT interlayers on uncured carbon/epoxy prepreg surfaces. Chemistry tuned compatibility of P(St-co-GMA) nano fibers with the epoxy matrix and its ability to confine MWCNTs were assessed. Three point bending test results showed significant amount of increase in both flexural strength and flexural modulus up to 25% and 29% respectively. The mode II delamination resistance was increased up to 70% and noticeable changes in the fracture modes were observed when nanocomposite interlayers were incorporated into the laminates. The resistance against transverse matrix cracking was tested under impact and tension loads. Interlayered charpy impact specimens absorbed 20% more energy than the non-interlayered ones. Transverse tensile strength of the interlayered UD specimens was about 27% higher than the non-interlayered specimens. Cross sectional fracture surface analysis suggested compatibility of interlayers with the surrounding matrix, which we attributed as the reason for resistance against matrix cracking. Chemical characteristics with the choice of P(St-co-GMA) also enable the incorporation of MWCNTs during electrospinning, which eventually increased further the mechanical performance of the interlayered laminates with a very low weight penalty (at about 0.2% by a single fibrous layer).

2.5 References

- [1] T.K. Tsotsis, "Interlayer toughening of composite materials", *Polymer Composites*, 30(1):70–86, 2009
- [2] J.S. Kim, D.H. Reneker, "Mechanical properties of composites using ultra fine electrospun fibers", *Polymer Composites*, 20(1):124–31, 1999
- [3] Y. Dzenis, D.H. Reneker, "Delamination resistant composites prepared by small diameter fiber reinforcement at ply interfaces", USPATENT 626533, 2008
- [4] Y. Dzenis, "Structural nanocomposites", *Science*, 319(5862):419–20, 2008
- [5] S. Sihn, R.Y. Kim, W. Huh, K.H. Lee, A. K. Roy, "Improvement of damage resistance in laminated composites with electrospun nano-interlayers. *Compos Sci Technol*, 68(3-4):673–83, 2008
- [6] L. Liu, Z.M. Huang, C. He, X. Han, "Mechanical performance of laminated composites incorporated with nanofibrous membranes.", *Materials Science and Engineering*; ,435-436(0):309–17,
- [7] L. Liu, Z.M. Huang, G.Y. Xu, Y.M. Liang, G.H. Dong, "Mode II interlaminar delamination of composite laminates incorporating with polymer ultra thin fibers." *Polymer Composites*;29(3):285–92, 2008
- [8] S.H. Lee, J.H. Lee, S.K. Cheong, N. Noguchi "A toughening and strengthening technique of hybrid composites with non-woven tissue", *Journal of Materials Processing Technology*;207(1-3):21–9, 2008
- [9] S.H. Lee, H. Noguchi, Y.B. Kim, S.K. Cheong "Effect of interleaved non woven carbon tissue on interlaminar fracture toughness of laminated composites: Part 1: mode II.", *JComposMater*;36(18):2153–68, 2002
- [10] A. Zucchelli, C. Gualandi, M.L. Focarete, L. Donati, G. Minak, S.

- Ramakrishna "Influence of electrospun Nylon 6,6 nanofibrous mats on the interlaminar properties of Gr-epoxy composite laminates", *Composite Structures*;94(2);571-79,2012
- [11] A. Zucchelli, M.L Focarete, C.Gualandi, S. Ramakrishna, "Electrospun nanofibers for enhancing structural performance of compositmaterials." , *Polymers for Advanced Technologies*;22(3):339–49,2011
- [12]E. T.Thostenson, W.Z.Li, D.Z.Wang, Z.W Ren, T.W.Chou, "Carbon nanotube/carbon fiber hybrid multiscale composites" *J. Appl. Phys*;91, 6034-37,2002
- [13]H.Qian, E.S.Greenhalgh, M.S.P Shaffer, A.Bismarck , "Carbon nanotube based hierarchical composites: A review" , *J Mater Chem*, 2010;20(23):4751–62.
- [14] Q.H. Zeng, A.B. Yu, G.Q.Lu, "Multiscale modeling and simulation of polymer nanocomposites", *Prog. Polym. Sci.*, 33: 191–269, 2008
- [15] H.Hu, L.Onyebueke, A.Abatan, "Characterizing and Modeling Mechanical Properties of NanocompositesReview and Evaluation", *Journal of Minerals & Materials Characterization & Engineering*, 9;4;275,2010
- [16] J. LLorca,C. González, J. M. Molina-Aldareguía, J. Segurado, R. Seltzer, F. Sket , M. Rodríguez, S. Sádaba, R. Muñoz, and L. P. Canal, "Multiscale Modeling of Composite Materials: a Roadmap Towards Virtual Testing", *Adv. Mater.*;23: 5130 47,2011
- [17] M.R Loos., K.Schulte, "Is It Worth the Effort to Reinforce Polymers With Carbon Nanotubes? ", *Macromol. Theory Simul.*; 20: 350–62,2011
- [18] E. Ozden, Y.Z Menciloglu, M.Papila, "Engineering chemistry of electrospun nanofibers and interfaces in nanocomposites for superior mechanical properties" *ACS Applied Materials and Interfaces*; 2(7):1788–93,2010
- [19] E.Ozden, Y.Z Menciloglu, M.Papila, "Electrospun Polymer/Carbon

Nanotubes nanofibers reinforced composites." *In:MaterialsResearchSociety Proceedings*. 2009

[20] H. Albertsen , J.Ivens, P.Peters, M.Wevers , I.Verpoest"Interlaminar fracture toughness of CFRP influenced by fibre surface treatment: Part I experimental results" , *Compos Sci and Technol*;54(2):133–45,1995

[21] E.Ozden-Yenigun, Y.Z. Menciloglu, M.Papila "MWCNTs/P(St-co-GMA) composite nanofibers of engineered interface chemistry for epoxy matrix nanocomposites. " *ACS Applied Materials &Interfaces*;4(2):777-784,2011

[22] X.J. Feng, L.Jiang, "Design and Creation of Super wetting/Anti wetting Surfaces. " , *Advanced Materials*; 18(23):3063–78,2006

[23] A.T.Seyhan, M.Tanoglu, K.Schulte, "Mode I and Mode II fracture toughness of e-glass non-crimp fabric/carbon nanotube(CNT) modified polymer based composites. " *Eng. Fracture Mechanics*; 75(18):5151-62,2008

[24] D.Stevanovic, S.Kalyanasundaram, A.Lowe, P.Y.Jar, "Mode I and Mode II delamination properties of glass/vinyl-ester composite toughened by particulate modified interlayers. " *Compos Sci and Technol*; 63(13):1949–64, 2003

CHAPTER 3

MICRO-MACRO

SURROGATE MODELS ON MICROMECHANICS BASED STRESS AMPLIFICATION FACTORS FOR CARBON FIBER REINFORCED/EPOXY COMPOSITE MATERIALS

3.1 Introduction

Besides the research efforts towards enhancing the mechanical response of composite materials (e.g. Chapter 2), substantial amount of efforts have been given to the effective implementation of these materials to the structural design cycles.

The structural design of composites typically requires a choice of failure criteria which is still open to discussion despite substantial amount of work carried out as overviewed in World Wide Failure Exercise[1]. The main difficulty for the failure criteria for composites is due to existence of multitude of failure mechanisms associated with the phases within the composite multi-scale architecture unlike traditional isotropic materials. Available and often considered as traditional failure criteria typically make use of macro lamina level strains and stresses. Their effectivity and prediction capabilities, however, may depend on the problem and the materials [2-22].

Contrary to the macro level approaches, the micromechanical methods explaining the effect of constituent properties on the micro level stress distributions were actively used till 2000[23-24]. Hyer and Waas [25] proposed first, capability of analytical models that are obtained from simple micromechanical models on the prediction of effective ply properties. This idea has been extended with the contributions of Hashin and Rosen [26]. Although analytical approaches granted successful expressions, the idealistic assumptions that they are based on usually limits their predictive capabilities under more general conditions. A step forward is the use of finite elements (FE) based approaches.

New generation failure criteria have aimed to implement accurately computed micro stresses and strains from the detailed analyses taking the multiphase nature of the material into account, such as FE based representative volume elements to the general prediction processes. Multi continuum model based on volume averages of micro stresses on different constituent phases, proposed by Mayes and Hensen [27-28] showed a reasonable way to implement the constituent properties to the general failure criteria. However, the volume averaging technique was found to be insufficient on the distinction of fiber/matrix interface failure and on the calculation of maximum stresses. In the studies of Ha et. al, [29-30] the isolated unit strain cases were applied to the FE based representative volume element (RVE) in order to extract the mechanical stress amplification factors (M_{σ}) from the specified critical points on the RVE rather than calculating the volume average stresses on the constituents. These factors create a bridge between the local micro stresses and general macro stresses and grants the direct implementation of micro stresses to the failure criteria. Several works have claimed the efficiency of MMF in the life and strength predictions of the composite materials under different loading conditions. Several of these studies have been put together by Tsai et al. [31].

Although it was shown as accurate, the implementation of MMF requires detailed FE analyses on RVE for given material property combination. This requirement may limit the use of MMF in easy implementation through the structural design cycles. As a black box solution to the problem, this study offers response surface based surrogate models for the calculation of stress amplification factors for carbon fiber reinforced epoxy composites. Two major constituent properties such as longitudinal fiber stiffness (E_f), isotropic matrix stiffness (E_m) and a lamina property such as fiber volume fraction (V_f) were chosen as influential factors for the micromechanics analyses. The ranges of the factors were chosen so that it covers most of the industrial carbon fiber and epoxy products manufactured by conventional composites manufacturing methods (Figures 3.2 -3.3). A three level full factorial experiment design with total 27 design points was considered. The combination of factors were assigned to the square array RVEs to which unit strain cases were applied under periodic boundary conditions. The extraction of stress amplification factor matrices was done as proposed by Ha et. al. [30]. Each index of M_{σ} matrix was represented by a second-degree polynomial function. Surrogate models for 5 distinct critical points on RVE were calculated and reported.

3.2 Methodology

3.2.1 Concept of “Experiment”

In the scope of this work, “experimentation” refers to the FE micromechanics computation process that leads to the extraction of critical stress amplification factors on the constituents. The process has the following set of actions. (I) creation of square array RVEs, (II) application of unit strains to RVEs that are subject to periodic boundary conditions, (III) evaluation of stress distributions on the critical points defined on the RVE. (IV) calculation of critical (maximum) stress amplification factors.

3.2.2 Planning and Analysis of Experiments: Response Surface Methodology

Investigation of the effect of the factors on the results usually requires number of different trials which changes both with number of factors or variables and their selected levels of interest. The planning and analyses of those runs/experiments were performed within the context of Response Surface Methodology. Response surfaces are used to approximate the numerical data as surrogate models which are usually low-order polynomials. The three key steps of the methodology as noted in [32] are following:

3.2.2.1 Design of Experiments

Parameter or factor settings for the experimentation (here the FEA based computations) were pre-selected. The selection represents the design/parameter space so that the experimentation will yield adequate and reliable measurements/calculations of the response of interest. Throughout this work a three-level factorial design was considered. Three-levels for each design variable were decided to be the bounds and the corresponding middle point. In total 3^3 design/test points were obtained for each design variable having three different levels. Any variable within the design domain may be represented in the coded domain with the following conversion function :

$$x_i = \frac{v_i - [\max(v_i) + \min(v_i)]/2}{[\max(v_i) - \min(v_i)]/2}$$

where x_i represents the coded value of the design variable when it takes the value v_i within the range of $\max(v_i)$ and $\min(v_i)$. With that representation the maximum, minimum and middle values were represented as 1,-1,0 respectively (Figure 3.1)

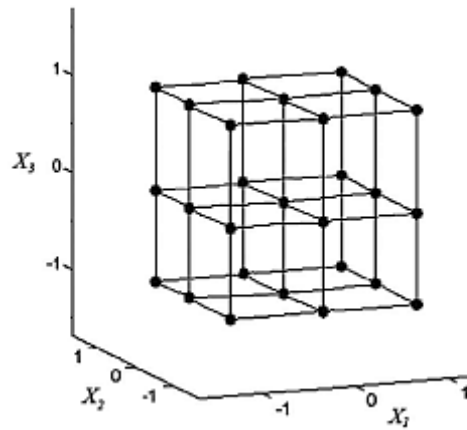


Figure 3.1: A three level full factorial cuboidal design in coded domain

3.2.2.2 Determination of Parameter Ranges

In the course of the determination of parameter or factor ranges, the basis was to create a broad design space so that aimed surrogate models would be valid for a wide range of composite material that can be formed of commercially available fiber/epoxy choices/combination.

From that perspective, as the first factor, E_F values were collected from the data sheets of well known carbon fiber filament manufacturers. Figure 3.2 shows the fiber stiffness, strength and diameter values for various carbon fiber filaments manufactured by Toray Carbon Fibers America Inc. [33] , Hexcel Composites Ltd. [34] and TOHO TENAX Co. Ltd. [35]. The shaded area in the figure nearly contains the whole range of available products. The minimum fiber stiffness value

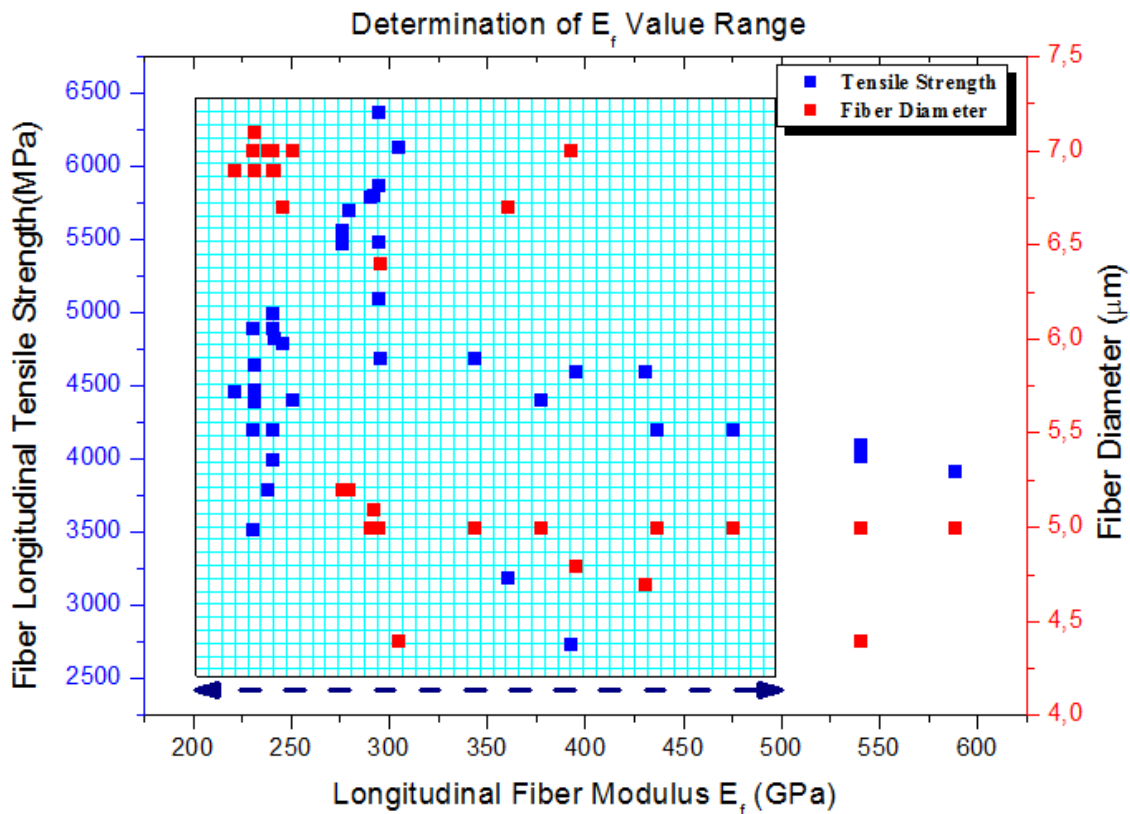


Figure 3.2: Fiber modulus and strength values for different carbon filament products.

reported was 221 GPa whereas the maximum stiffness was 588 GPa. Carbon fiber filaments having longitudinal stiffness values higher than 500 GPa may be considered as ultra high modulus fibers and their usage is limited to selective high-tech applications. Then, the practical bounds for E_f were decided to be 200 GPa and 500 GPa hence corresponding middle design point was 350 GPa. Also it is vital to address that the average fiber diameter values were either 5 μm or 7 μm . Since V_f was considered as another factor which contains the information about the fiber diameter when the modeling is carried out, the fiber diameter itself was not chosen as a specific factor, but its value was fixed to 5 μm .

While determining the matrix elastic modulus (E_M) range, several epoxy based prepreg data sheets provided by Hexcel Composites Ltd. [36] as well as the values reported by Soden et. al [37] were considered. Although the maximum value of the actual data was 5.1 GPa, the upper limit was set to 6 GPa so that associated parameter space would also cover stiffer epoxy products obtained with alteration of epoxy system (Figure 3.3). Minimum and the middle point for E_M was determined to be 3 and 4.5 GPa respectively. Since matrix phase was taken as an isotropic material, in plane shear

modulus have also changed with changing tensile modulus values where the in-plane Poisson's ratio (ν_{12}) was fixed to 0,35.

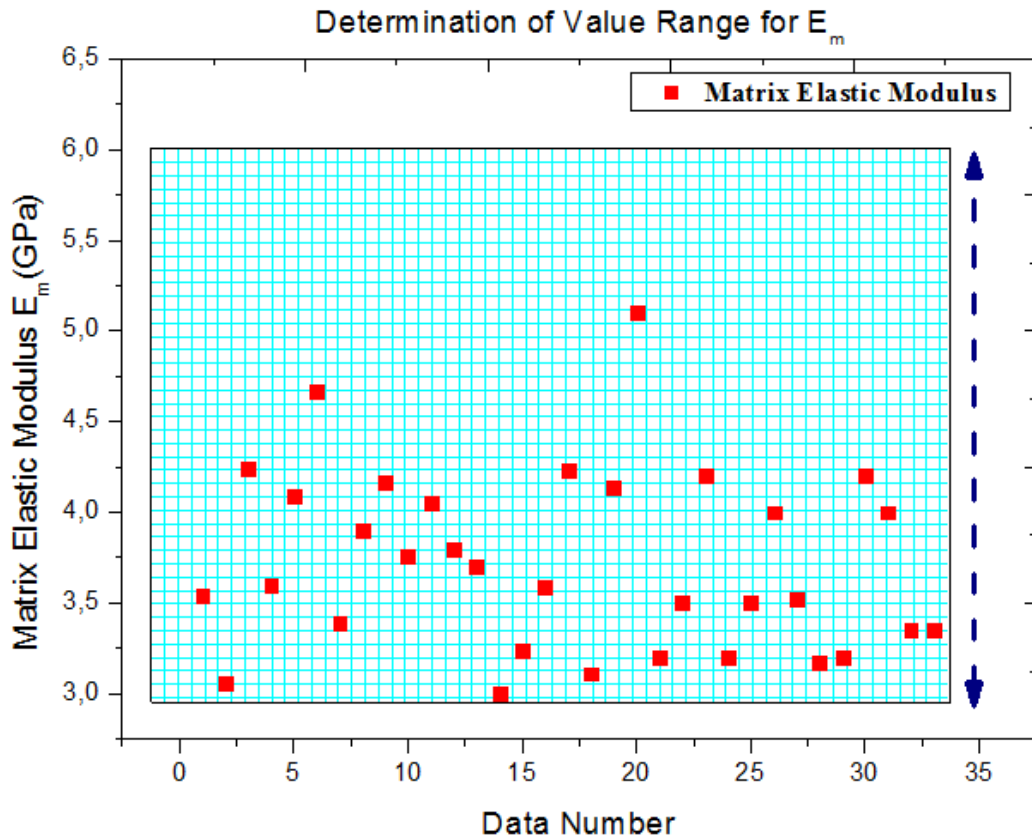


Figure 3.3: Elastic modulus values for different epoxy products.

From a parallel point of view, fiber volume fraction (V_f) was chosen to cover the typical range of composite products. In the determination of V_f the diversity of manufacturing methods was taken into account such that the minimum value was set to 40 % as an approximate value that may be obtained via a standard vacuum infusion process. The maximum value, however, was set to 70 % which was a reasonable value mostly achieved by the application of autoclaved pre-preg materials. The summary of used constituent properties were summarized in table 3.1 and 3.2

Table 3.1: Carbon fiber material data

Carbon Fiber (Anisotropic)	
Longitudinal Tensile Modulus E_f (GPa)	200-350-500
Transversal Tensile Modulus $E_{T2}=E_{T3}$ (GPa)	15.2
Major Poissons Ratio $\nu_{12}=\nu_{13}=\nu_{23}$	0.2
Minor Poissons Ratio $\nu_{21}=\nu_{31}$	0,015-0,008-0,006
In Plane Shear Modulus $G_{12}=G_{13}$ (GPa)	9.6
Out of Plane Shear Modulus G_{23} (GPa)	6.4
Volume Fraction (V_f)	0,4-0,55-0,7

Table 3.2: Epoxy material data

Epoxy (Isotropic)	
Elastic Modulus E_f (GPa)	3-4,5-6
Poisson's Ratio	0,35
Shear Modulus	2,02-3,04-4,05

3.2.2.3 Responses: Mechanical Stress Amplification Factors

Stress amplification factors were calculated by the same methodology proposed by Ha et. al [30] where 3 dimensional RVEs were subject to unit strains in 6 loading directions under periodic boundary conditions. A recapulation of this methodology is given in detail in the works of Ha [30] and also collected together by Firlar [38]. Responses that would be evaluated at each design point were the indices of M_σ matrix namely, $M_{\sigma_{xy}}$ values (Figure 3.4).

$$\begin{pmatrix} \sigma_1 = \sigma_{xx} \\ \sigma_2 = \sigma_{yy} \\ \sigma_3 = \sigma_{zz} \\ \sigma_4 = \sigma_{yz} \\ \sigma_5 = \sigma_{xz} \\ \sigma_6 = \sigma_{xy} \end{pmatrix}_j = \begin{bmatrix} M_{\sigma 11} & M_{\sigma 12} & M_{\sigma 13} & M_{\sigma 14} & 0 & 0 \\ M_{\sigma 21} & M_{\sigma 22} & M_{\sigma 23} & M_{\sigma 24} & 0 & 0 \\ M_{\sigma 31} & M_{\sigma 32} & M_{\sigma 33} & M_{\sigma 34} & 0 & 0 \\ M_{\sigma 41} & M_{\sigma 42} & M_{\sigma 43} & M_{\sigma 44} & 0 & 0 \\ 0 & 0 & 0 & 0 & M_{\sigma 55} & M_{\sigma 56} \\ 0 & 0 & 0 & 0 & M_{\sigma 65} & M_{\sigma 66} \end{bmatrix}_j \begin{pmatrix} \sigma_1 \\ \sigma_2 \\ \sigma_3 \\ \sigma_4 \\ \sigma_5 \\ \sigma_6 \end{pmatrix}$$

Figure 3.4: Mechanical stress amplification factor matrix acting on macro stresses.

The values of these factors were calculated at 6 critical points determined on the RVE, such as F1, F2, F3 (on fiber/matrix interface), IF1, IF2 and IS (on matrix) (Figure 3.5)

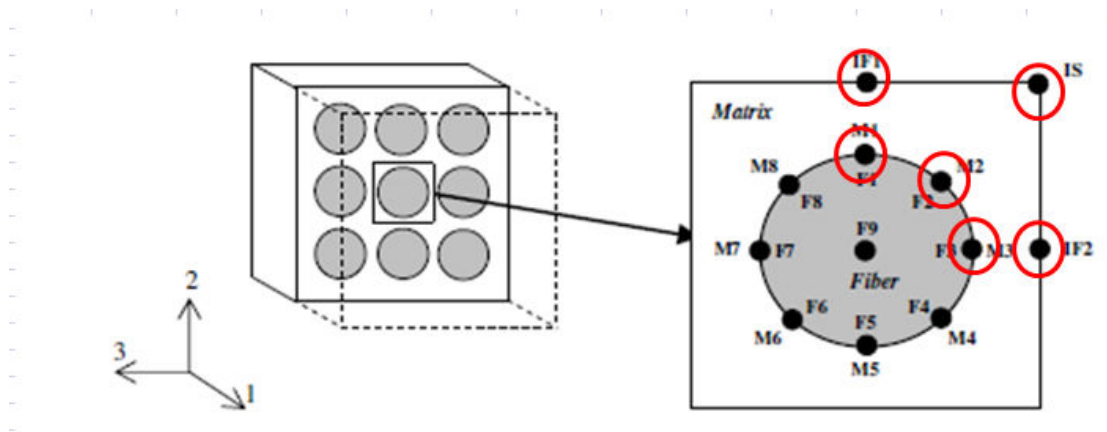


Figure 3.5 Square array fiber distribution and critical nodes.

3.2.2.4 Regression Analysis

Regression analysis were performed using Design Expert 8.2 by Stat-Ease which also conducts appropriate statistical tests concerning parameters in the mathematical model that is RS approximation. The fundamentals of least square fitting procedure and response surface analysis can be found in dedicated sources [39]. A stepwise regression based on backward elimination method was performed where all of the responses (b) were initially fit to a second order polynomial function (see figure 2.6) that was followed by the sequential elimination of “ least significant” factors determined by variance analysis. The significance level was determined to be 0.05 and each factor having a p-value higher than 0.05 was eliminated from the mathematical model. Approximated β parameters were obtained at the end of analysis.

$$\mathbf{y} \approx \beta_0 + \beta_1 x_1 + \beta_2 x_2 + \beta_3 x_3 + \beta_4 x_1 x_2 + \beta_5 x_1 x_3 + \beta_6 x_2 x_3 + \beta_7 x_1^2 + \beta_8 x_2^2 + \beta_9 x_3^2$$

where $x_1 = \mathbf{V}_f$, $x_2 = \mathbf{E}_f$, $x_3 = \mathbf{E}_m$,

3.3 Results and Discussion

3.3.1 Verification of FE Based Stress Analysis

Although the process of calculating the stress amplification factors was well defined in the literature, the extraction process is sensitive both to nature of the FE model (mesh type, element number) and to the solver used for the FE analysis.

The verification was evaluated through an example case that was both studied by Tay and Yudhanto [39] and Ha [30]. The material properties used in this example case is shown in table 3.3. This example case was specifically chosen so that the material properties were within in the selected parameter space.

Table 3.3: Ply properties for the example case studied ($V_f=0,7$)

Fiber (Graphite: IM7)	Magnitude
Axial modulus E_{11f} , in GPa	303
Transverse modulus E_{22f} ($= E_{33f}$), in GPa	15.2
Shear modulus G_{12f} ($= G_{13f}$), in GPa	9.65
Shear modulus G_{23f} , in GPa	6.32
Poisson's ratio ν_{12f} ($= \nu_{13f} = \nu_{23f}$)	0.2
Coefficient of thermal expansion α_{11f} , in /deg C	0.0
Coefficient of thermal expansion α_{22f} ($= \alpha_{33f}$), in $\mu\epsilon/\text{deg C}$	8.28
Matrix (Epoxy)	
Young's modulus E_m , in GPa	3.31
Shear modulus G_m , in GPa	1.23
Poisson's ratio ν_m	0.35
Coefficient of thermal expansion α_m , in $\mu\epsilon/\text{deg C}$	57.6

By assigning these material properties to square RVEs and applying unit strains, Tay and Yudhanto [40] made a systematic investigation on the strain amplification factors. For the verification case, the major amplification factors at the orthogonal of strain amplification factor matrix at the studied critical points were considered. A comparison of the strain amplification values found in Tay's work and current study is given in Table 3.4.

Table 3.4: Comparison of strain amplification factors at different critical points

Current Work	S11	S22	S33	S12	S23	S13
F1	1,000	0,952	0,454	0,864	0,706	0,388
F2	1,000	0,634	0,634	0,507	0,630	0,507
F3	1,000	0,454	0,952	0,388	0,698	0,864
IF1	1,000	2,995	0,371	7,470	3,686	0,278
IF2	1,000	0,371	2,995	0,378	3,704	7,470
IS	1,000	1,097	1,097	1,780	2,426	1,780
Tay and Yudhanto						
F1	1,000	0,970	0,435	0,902	0,692	0,355
F2	1,000	0,631	0,631	0,510	0,678	0,510
F3	1,000	0,435	0,970	0,355	0,692	0,902
IF1	1,000	3,156	0,339	7,502	3,747	0,266
IF2	1,000	0,339	3,165	0,266	3,747	7,502
IS	1,000	1,050	1,050	1,799	2,780	1,799

The comparison of the strain amplification factor values indicated the correct application of unit strains and periodic boundary conditions to RVEs. Figures 3.6a-3.6f corresponds to the correct strain distribution on RVE.

Further verification was done by calculating the effective ply properties out of the macro compliance matrix obtained by the volume average of stresses on the RVE. The elastic ply properties calculated were compared by the ones that have been reported by Ha et. Al [30] (Table 3.5).

Table 3.5: Comparison of effective property predictions

	Current	Ha
E_{11} (GPa)	212,58	≈ 210
E_{22} (GPa)	9,89	≈ 10
E_{33} (GPa)	9,89	≈ 10
G_{23} (GPa)	3,06	≈ 3
G_{13} (GPa)	4,44	$\approx 4,5$
G_{12} (GPa)	4,43	$\approx 4,5$
ν_{12}	0,24	$\approx 0,22$
ν_{23}	0,3	$\approx 0,2$

These results confirmed that the overall process implemented here equally well and current models may be used in the extraction of M_6 matrices.

After this correlation, next step was to solve each 6 models for each point determined by the experiment design and to collect and evaluate the stress amplification factors in each critical point.

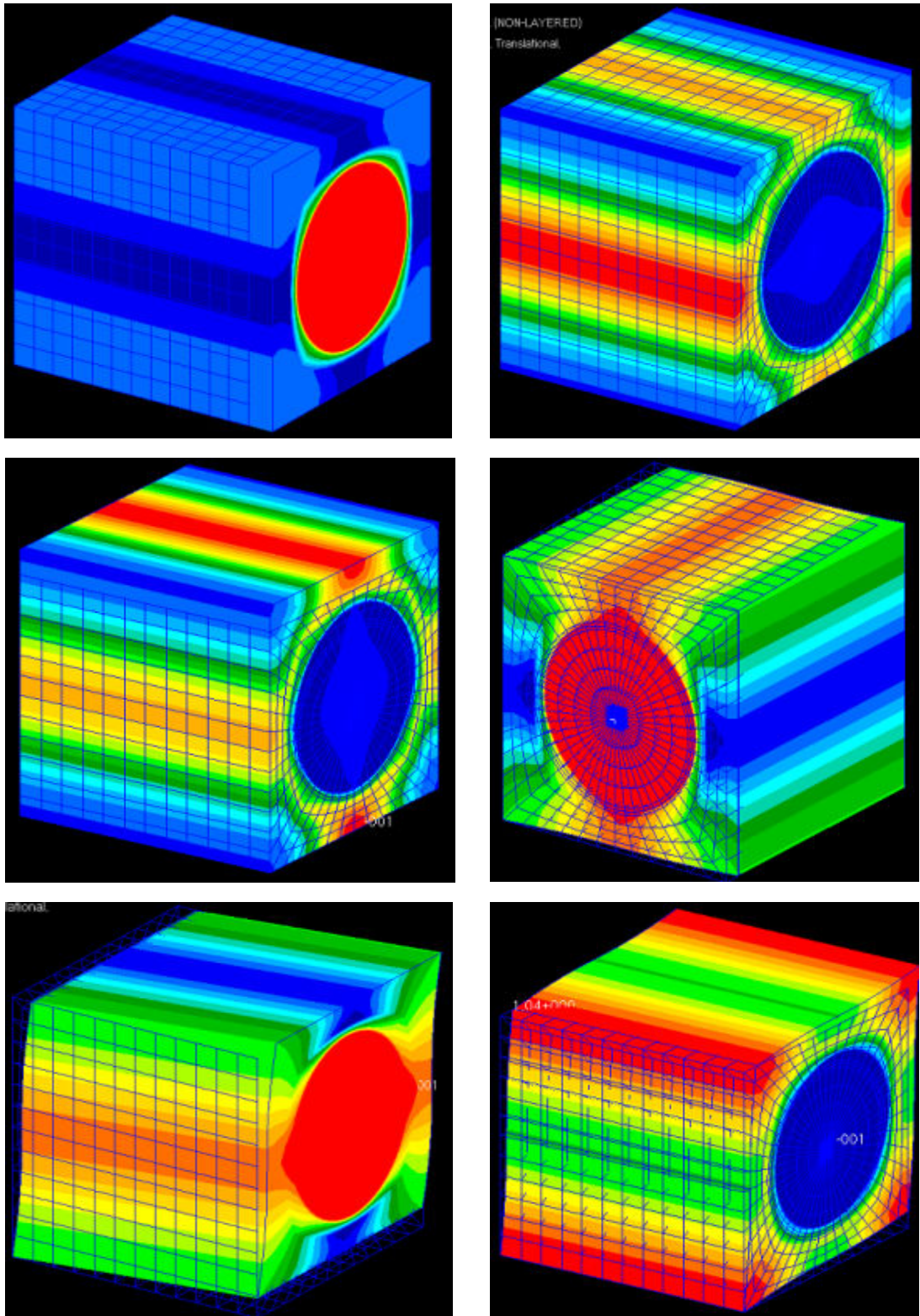


Figure 3.6 RVEs subjected to unit strains a) 11 direction b) 22 direction c) 33 direction d) 13 direction e) 12 direction f) 23 direction

3.3.2 Surrogate Models for Stress Amplifications on Fiber/Matrix Interface (F1, F2, F3) and Matrix Phase (IF1, IF2, IS)

Stress amplification factors on the fiber phase were determined from the critical points F1, F2, and F3. Also note the fact that due to transversely isotropic nature of the lamina along with the symmetry of the RVE, the radial strains at point F1 and F3 are also equal (e.g. M_{22} on the critical point F1 are the same with M_{33} on F3) In order to avoid unnecessary calculations, the surrogate models were calculated for F1 by which F3 can be adopted, and for F2 separately (Table 3.6 and Table 3.7). Similarly stress amplification factors on the matrix phase were determined from the critical points IF1, IF2, and IS . In order to avoid unnecessary calculations, the surrogate models were used together for IF1 and IF2 whereas IS was reported separately (Table 3.8 and Table 3.9). Critical fiber stress amplification factors would then be determined by taking the maximum value of each term on different critical points. The empty spaces in the tables, correspond to the statistically insignificant terms which were eliminated during stepwise regression process.

Table 3.6: Non-zero Coefficients β_s determined by stepwise regression for M_σ matrix on critical point F1

	β_0 (Intercept)	β_1 (V_f)	β_2 (E_f)	β_3 (E_m)	β_4 (V_f)*(E_f)	β_5 (V_f)*(E_m)	β_6 (E_f)*(E_m)	β_7 (V_f) ²	β_8 (E_f) ²	β_9 (E_m) ²
$M\sigma_{11}$	1,799	-0,515	0,011	-0,007	-0,007			0,138		
$M\sigma_{22}$	1,279	0,010		-0,101		-0,037				0,014
$M\sigma_{33}$	1,003	-0,173		0,030		0,044		-0,035		-0,006
$M\sigma_{44}$	1,138	0,109		-0,051		-0,036		0,083		
$M\sigma_{55}$	1,017	-0,175		0,004		0,016		0,012		
$M\sigma_{66}$	1,528	0,143		-0,082		-0,038		0,093		
$M\sigma_{12}$	-0,212	0,159	-0,003	-0,031		-0,013		-0,047		0,003
$M\sigma_{13}$	-0,210	0,157	-0,003	0,009	0,002	0,009		-0,048		-0,002
$M\sigma_{21}$	-0,007									
$M\sigma_{31}$	-0,007									
$M\sigma_{23}$	-0,056	0,065		-0,005		-0,027		-0,009		
$M\sigma_{32}$	-0,110	0,123		-0,006		-0,010		0,084		0,002

Table 3.7: Non-zero Coefficients β_s determined by stepwise regression for M_σ matrix on critical point F2

	β_0 (Intercept)	β_1 (V_f)	β_2 (E_f)	β_3 (E_m)	β_4 (V_f)*(E_f)	β_5 (V_f)*(E_m)	β_6 (E_f)*(E_m)	β_7 (V_f) ²	β_8 (E_f) ²	β_9 (E_m) ²
Mσ_{11}	1,801	-0,514	0,013	-0,008	-0,009	0,006		0,138	-0,004	
Mσ_{22}	1,059	-0,103		-0,002		0,030		0,005		-0,005
Mσ_{33}	1,059	-0,103		-0,002		0,030		0,005		-0,005
Mσ_{44}	1,211	0,023		-0,042		-0,007		-0,004		0,003
Mσ_{55}	1,222	-0,123		-0,014		0,014				
Mσ_{66}	1,222	-0,123		-0,014		0,014				
Mσ_{12}	-0,212	0,156	0,004	-0,006	0,004	0,002	-0,002	-0,047	0,002	
Mσ_{13}	-0,212	0,156	0,004	-0,006	0,004	0,002	-0,002	-0,047	0,002	
Mσ_{21}	-0,007									
Mσ_{31}	-0,007									
Mσ_{23}	-0,052	0,075	0,001	-0,015		-0,014		0,33		0,004
Mσ_{32}	-0,052	0,075	0,001	-0,015		-0,014		0,33		0,004
Mσ_{24-34}	-0,116	0,111		0,003		-0,067		0,165		
Mσ_{42-43}	-0,048	0,057		-0,001		-0,012		0,076		
Mσ_{56-65}	-0,212	0,219						0,311		

Table 3.8: Non-zero Coefficients β_s determined by stepwise regression for M_σ matrix on critical point IF1

	β_0 (Intercept)	β_1 (V_f)	β_2 (E_f)	β_3 (E_m)	β_4 (V_f)*(E_f)	β_5 (V_f)*(E_m)	β_6 (E_f)*(E_m)	β_7 (V_f) ²	β_8 (E_f) ²	β_9 (E_m) ²
$M\sigma_{11}$	0,026	-0,008	-0,014	0,010	0,003	-0,003	-0,005	0,002	0,006	
$M\sigma_{22}$	1,237	-0,029		-0,113		-0,048				0,024
$M\sigma_{33}$	0,534	-0,202		0,104		0,016		0,005		
$M\sigma_{44}$	0,885	0,246		-0,027		-0,053		0,080		
$M\sigma_{55}$	0,186	-0,086		0,052		-0,004		0,032		
$M\sigma_{66}$	1,336	0,241		-0,070		-0,050		0,095		
$M\sigma_{12}$	0,254	-0,018	0,004	-0,046	-0,002	-0,010	0,002		-0,002	0,004
$M\sigma_{13}$	0,258	-0,019	0,004	0,046		0,002				
$M\sigma_{21}$	0,011									
$M\sigma_{31}$	0,004									
$M\sigma_{23}$	0,141	0,196		0,029		-0,024		0,042		
$M\sigma_{32}$	0,013	0,101		-0,035		-0,016		0,028		-0,002

Table 3.9: Non-zero Coefficients β_s determined by stepwise regression for M_σ matrix on critical point IS

	β_0 (Intercept)	β_1 (V_f)	β_2 (E_f)	β_3 (E_m)	β_4 (V_f)*(E_f)	β_5 (V_f)*(E_m)	β_6 (E_f)*(E_m)	β_7 (V_f) ²	β_8 (E_f) ²	β_9 (E_m) ²
$M_{\sigma_{11}}$	0,027	-0,008	-0,014	0,010	0,003	-0,002	-0,004	0,002	0,006	
$M_{\sigma_{22}}$	0,647	-0,021		0,072		0,012		0,010		0,005
$M_{\sigma_{33}}$	0,647	-0,021		0,072		0,012		0,010		0,005
$M_{\sigma_{44}}$	1,066	-0,109		0,011				-0,030		
$M_{\sigma_{55}}$	0,608	-0,105		0,035		0,015		-0,015		
$M_{\sigma_{66}}$	0,608	-0,105		0,035		0,015		-0,015		
$M_{\sigma_{12}}$	0,257	-0,011	0,004	0,011	-0,001	0,006	0,001	0,008	-0,002	
$M_{\sigma_{13}}$	0,257	-0,011	0,004	0,011	-0,001	0,006	0,001	0,008	-0,002	
$M_{\sigma_{23}}$	0,285	0,009		-0,034		0,004				
$M_{\sigma_{32}}$	0,285	0,009		-0,034		0,004				

With the use of these functions stress amplification factors on the critical points may be calculated both for matrix and fiber phases.

3.3.3 Surrogate Model Adequacy Checking and Parameter Effects

Prediction accuracy of the surrogates can be evaluated by the comparison of actual and predicted values of M_{xy} at different critical points. For these comparisons, the diagonal terms of M_{σ} matrix at the critical points were primarily considered and reported here. Effect of parameters on the general responses can also be determined by the statistical tests of RSM on the coefficients along with their magnitudes associated with the coded domain.

For M_{11} the prediction results were in good agreement with the actual data and its magnitude was almost the same at F1, F2 and F3 critical points (Figure 3.7). Fiber volume fraction was the most effective parameter changing the values of M_{11} . Whereas E_f and E_m parameters had a relatively minor effect.

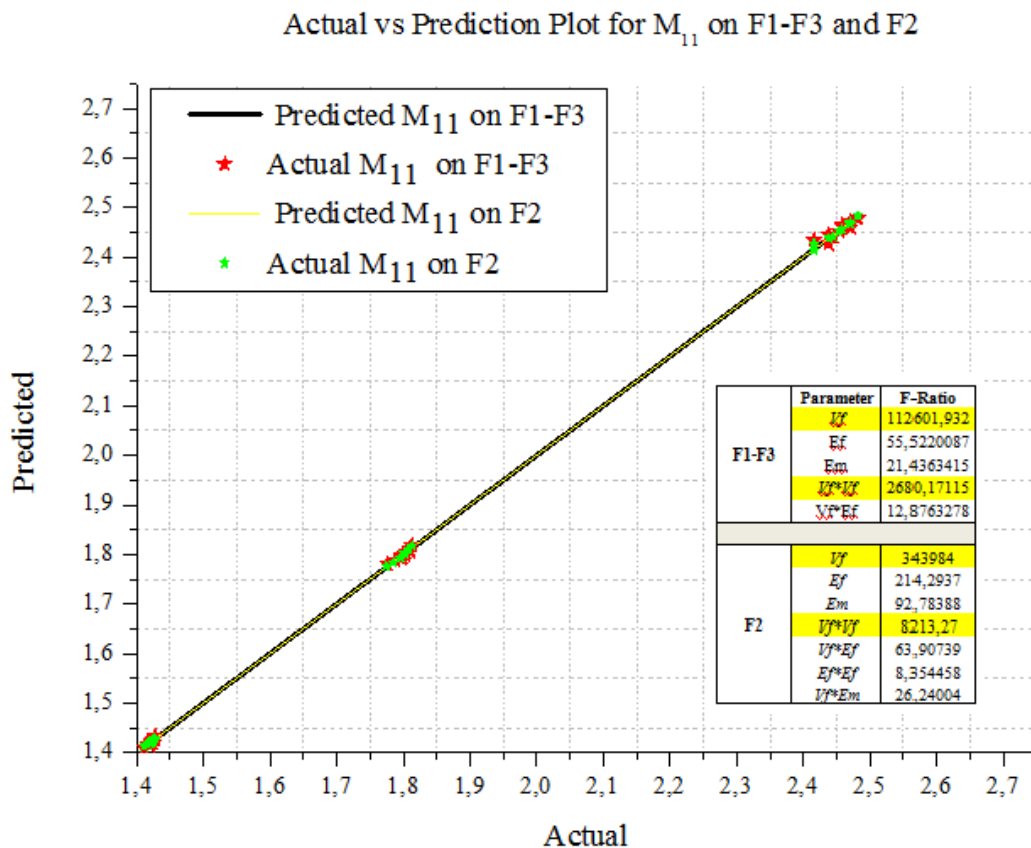


Figure 3.7 Actual vs. Prediction plot and F-Ratios for M_{11} on F1, F2, F3

The most critical point for M_{22} was F1. Depending on the parameter combinations the maximum value was changing between these two points. Actual vs. prediction plots suggested that the model adequacy was good ($R^2=0,99$). For this case the most significant parameter was E_m . The combined effect or interaction of V_f and E_m was also effective..

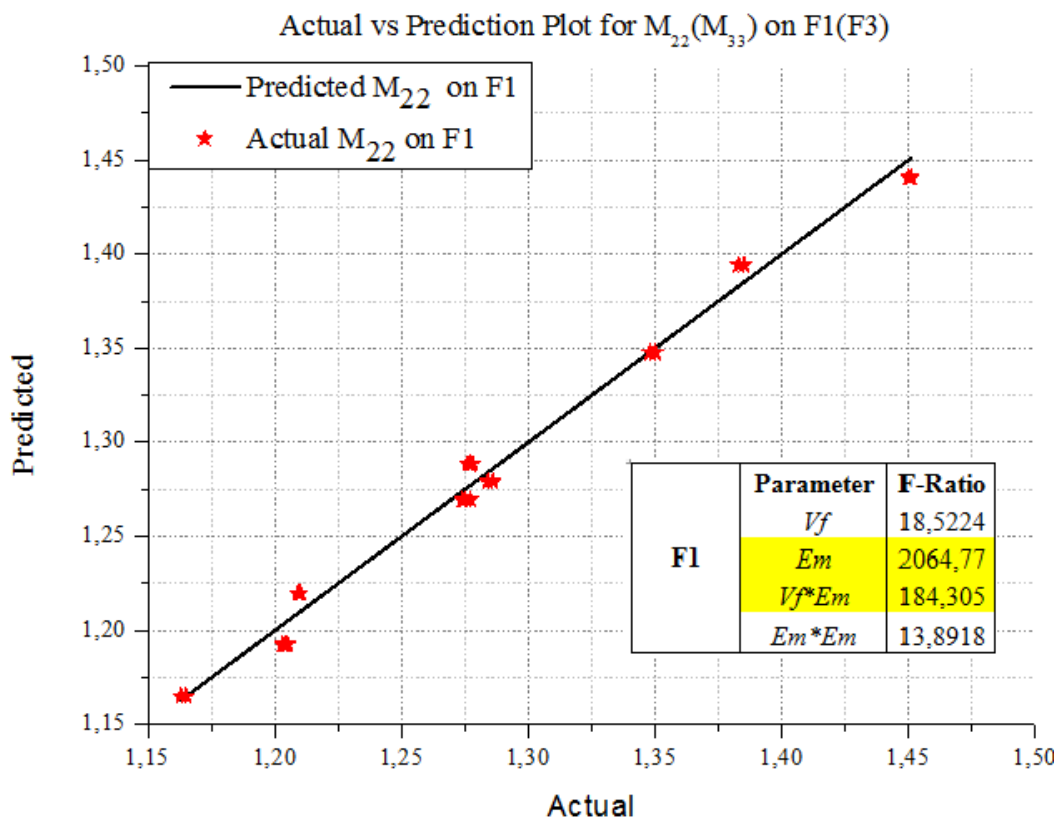


Figure 3.8 Actual vs. Prediction plot and F-Ratios for M_{22} on F1

In the case of M_{44} which corresponds to the critical stress amplification factor on 23 direction, the location of the critical was changing with the changing parameter combinations between the points F1 and F2. V_f was the most effective parameter along with E_m in both cases. For low volume fractions the stress concentration have appeared on F2 but with increasing V_f F1 becomes critically loaded. In addition to this the fit quality was in an acceptable range for both critical points.

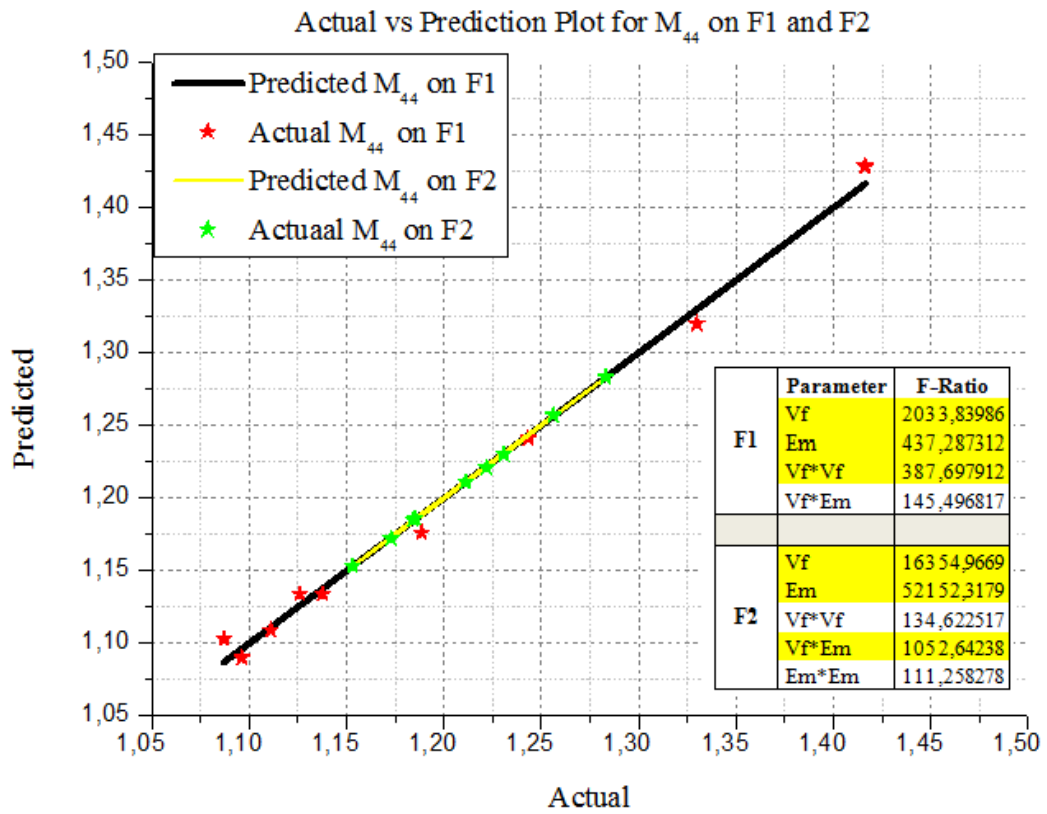


Figure 3.9 Actual vs. Prediction plot and F-Ratios for M_{44} on F1 and F2

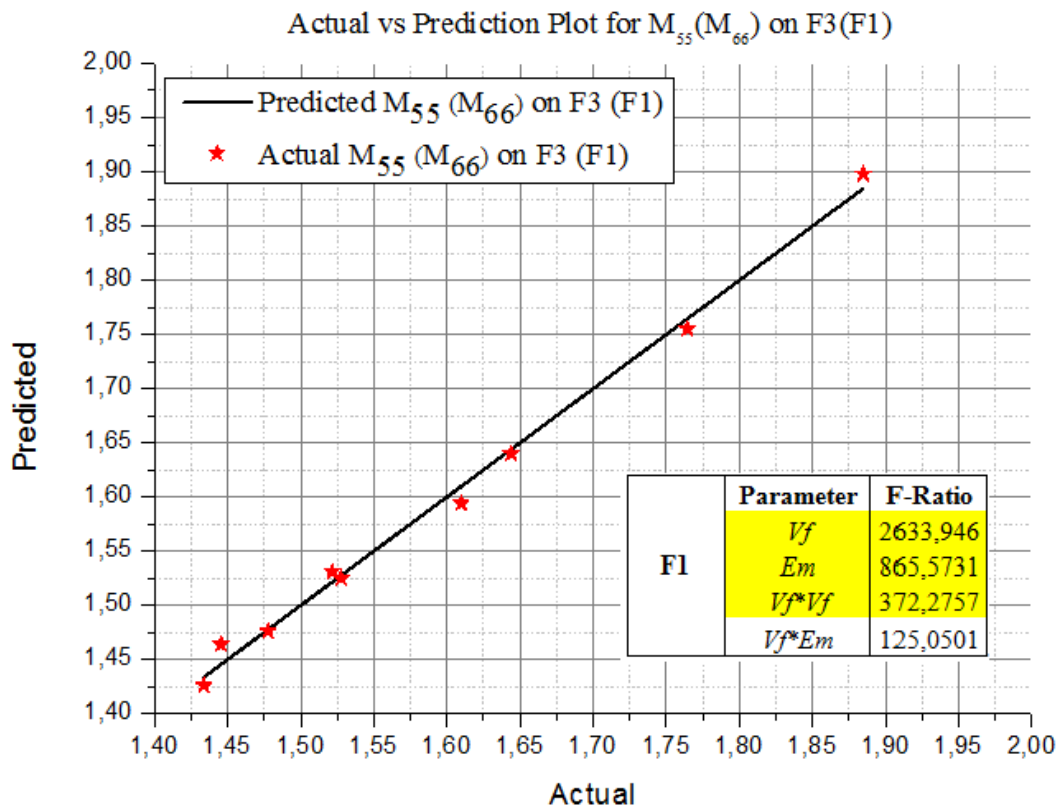


Figure 3.10: Actual vs. Prediction plot and F-Ratios for $M_{55}(M_{66})$ on F3 (F1)

In the case of M_{55} which corresponds to the critical stress amplification factor on 13 direction, F3 was the most critical point. V_f was the most effective parameter along with E_m in both cases. For low volume fractions the stress concentration have appeared on F2 but with increasing V_f F1 becomes critically loaded. In addition, the fit quality was in an acceptable range for both critical points.

3.4 Conclusion and Future Works

The conclusions and achievements to be underlined as a result of this chapter may be summarized as:

- Square array RVEs that were subjected to unit strains in six different loading directions under periodic boundary conditions, were created efficiently by using MSC PATRAN and solved by MD NASTRAN.
- 3 parameters namely longitudinal elastic modulus of fiber (E_f), fiber volume fraction (V_f) and elastic modulus of matrix (E_m) were chosen. The ranges of the parameters were determined through product data bases and literature search.
- An example case was studied, in order to justify the present FE models that were solved by MD NASTRAN. Present model results and referenced strain amplification values along with effective material property predictions correlated very well
- FE models were solved and post processed at 27 full factorial case points and stress amplification matrix for each case was calculated and noted.
- Every term in M_σ matrices at the previously determined critical points on RVE were represented as a surrogate quadratic polynomial function taking the design variables as internal parameters by response surface based regression analysis. Approximated values were reported
-

Beginning from this point the future directions for the current work may be listed as:

- The implementation of transversal elastic modulus of fibers as fourth design variable will be considered. Its effects on the reported values will be evaluated

- Approximation models will be used in the creation of MMF based failure bands where the effect of uncertainty on material properties will be studied through Vertex Method [41]. The requirement of FE analysis at each point determined by uncertainty limits will be replaced by the use of surrogate models.

3.5 References

- [1] Failure Criteria in Fibre Reinforced Polymer Composites: The World-Wide Failure Exercise, edited by M.J. Hinton, A.S. Kaddour, P.D. Soden, Elsevier (2004)
- [2] Azzi, V.D. and Tsai, S.W. Anisotropic Strength of Composites, *Experimental Mechanics*, 5: 283–288, 1965
- [3] Tsai, S.W. Strength Characteristics of Composite Materials, *NASA Contractor Report, CR-224, National Aeronautics and Space Administration*, 1965
- [4] Tsai, S.W. and Wu, E.M. A General Theory of Strength for Anisotropic Materials, *Journal of Composite Materials*, 5: 58–80, 1971
- [5] Hashin, Z. and Rotem, A. (1973). A Fatigue Failure Criterion for Fiber Reinforced Materials, *Journal of Composite Materials*, 7: 448–464, 1973
- [6] Hashin, Z. , Failure Criteria for Unidirectional Fiber Composites, *Journal of Applied Mechanics*, 47: 329–334, 1980
- [7] Yamada, S.E. and Sun, C.T. , Analysis of Laminate Strength and Its Distribution, *Journal of Composite Materials*, 12: 275–284, 1978
- [8] Chang, F.K., Scott, R.A. and Springer, G.S, Failure of Composite Laminates Containing Pin Loaded Holes — Method of Solution, *Journal of Composite Materials*, 18: 255–278, 1984
- [9] Chang, F.K., Scott, R.A. and Springer, G.S. , Failure Strength of Nonlinearly Elastic Composite Laminates Containing Pin Loaded Holes — Method of Solution, *Journal of Composite Materials*, 18: 464–477, 1984
- [10] Chang, F.K. and Chang, K.Y, A Progressive Damage Model for Laminated Composites Containing Stress Concentrations, *Journal of Composite Materials*, 21: 834–855, 1987.

- [11]Hart-Smith, L.J. , A New Approach to Fibrous Composite Laminate Strength Prediction. *Eighth DOD/NASA/FAA Conference on Fibrous Composites in Structural Design, NASA CP-3087*, Part 2: 663–693, 1989
- [12]Feng, W.W. , A Failure Criterion for Composite Materials. *Journal of Composite Materials*, 25: 88–100, 1991.
- [13]Pang, S., Pandian, A. and Bradshaw, R.D. , Modified Tsai-Wu Failure Criterion for Fiber-Reinforced Composite Laminates,*Polymer Composites*, 13(4): 273–277, 1992.
- [14]Shahid, I. and Chang, F.K. , Failure and Strength of Laminated Composite Plates under Multiple In-Plane Loads, *38th International SAMPE Symposium*: 967–977, 1993.
- [15]Shahid, I. and Chang, F.K.. An Accumulative Damage Model for Tensile and Shear Failures of Laminated Composite Plates, *Journal of Composite Materials*, 29(7): 926–981, 1995
- [16]Chandler, H.D., Campbell, I.M.D. and Stone, M.A. . An Assessment of Failure Criteria for Fiber Reinforced Composite Laminates. *International Journal of Fatigue*, 17(7): 513–518, 1995
- [17] Christensen, R.M. , Stress based Yield/Failure Criteria for Fiber Composites, *International Journal of Solids and Structures*, 34(5): 529–543, 1997
- [18] Deng, S. and Ye, L. , Influence of Fiber–matrix Adhesion on Mechanical Properties of Graphite/Epoxy Composites: I. Tensile, Flexure, and Fatigue Properties, *Journal of Reinforced Plastics and Composites*, 18: 1021–1040, 1999
- [19]Deng, S. and Ye, L. , Influence of Fiber–matrix Adhesion on Mechanical Properties of Graphite/Epoxy Composites: II. Interlaminar Fracture and Inplane Shear Behavior, *Journal of Reinforced Plastics and Composites*, 18: 1041–1057, 1999

- [20] Deng, S. and Ye, L. , Influence of Fiber–matrix Adhesion on Mechanical Properties of Graphite/Epoxy Composites: III. Impact and Dynamic Mechanical Properties, *Journal of Reinforced Plastics and Composites*, 19: 689–703, 1999
- [21] Kim, K.Y. and Ye, L. , Influence of Matrix and Interface on Transverse Mechanical Properties of CF–PEI Thermoplastic Composites at Elevated Temperatures, *Journal of Reinforced Plastics and Composites*, 24: 429–445,2005
- [22] Hobbiebrunken, T., Hojo, M., Adachi, T., Jong, C.D. and Fiedler, B. , Evaluation of Interfacial Strength in CF/Epoxy using FEM and In-Situ Experiments, *Composites Part A: Applied Science and Manufacturing*, 37(12): 2248–2256, 2006
- [23] S. K. Ha, K. K. Jin and Y. Huang, “Micro-Mechanics of Failure (MMF) for Continuous Fiber Reinforced Composites,” *Journal of Composite Materials*, 2008.
- [24] K-K. Jin, Y. Huang, Y-H Lee and S. K HA, “Distribution of Micro Stresses and Interfacial Traction in Unidirectional Composites,” *Journal of Composite Materials*, 2008.
- [25] Hyer, M. W. And Waas, A. M. (2000). Micromechanics of Linear Elastic Continuous Fiber Composites, In: *Comprehensive Composite Materials*, 345-375, Elsevier, Oxford.
- [26] Hashin, Z. and Rosen, B.W. (1964). The Elastic Moduli of Fiber-Reinforced Materials, *ASME Journal of Applied Mechanics*, 31: 223-232.
- [27] Mayes, J.S. (1999). Micromechanics Based Failure Analysis of Composite Structural Laminates, Carderock Division, Naval Surface Warfare Center, Ship Structures and Materials Department, NSWCCD-65-TR-1999/15.
- [28] Mayes, J.S. and Hansen, A.C. (2004). A Comparison of Multicontinuum Theory based Failure Simulation with Experimental Results, *Composites Science and Technology*, 64 (3–4): 517–527.

- [29] S. K. Ha, K. K. Jin and Y. Huang, “Micro-Mechanics of Failure (MMF) for Continuous Fiber Reinforced Composites,” Journal of Composite Materials, 2008.
- [30] K-K. Jin, Y. Huang, Y-H Lee and S. K HA, “Distribution of Micro Stresses and Interfacial Traction in Unidirectional Composites,” Journal of Composite Materials, 2008.
- [31] S.W.Tsai, Strength and Life of Composites, JEC Composites, 2008
- [32] O.S Yordem, M.Papila, Y.Z Menciloglu , “ Effects of Electrospinning Parameters on Polyacrylonitrile Nanofiber Diameter: An Investigation by Response Surface Methodology, Materials & Design, 26(1):33-44, 2008
- [33] TORAY Carbon Fibers America, Product Data Sheets for Carbon Fiber Filaments, Retrieved online from <http://www.toraycfa.com/product.html>, May 2012.
- [34] Hexcel Composites Ltd., Product Data Sheets for Carbon Fiber Filaments, Retrieved online from <http://www.hexcel.com/Resources/Cont-CarbonFiberDataSheets>, May 2012
- [35] TOHO TENAX Co. LTD. , Product Data Sheets for Carbon Fiber Filaments, Retrieved online from http://www.tohotenax.com/tenax/en/products/st_property.php , May 2012
- [36] Hexcel Composites Ltd., Product Data Sheets for Prepreg Materials, Retrieved online from <http://www.hexcel.com/Resources/prepreg-data-sheets> , May 2012
- [37] Soden, P.D., Hinton, M.J. and Kaddour, A.S. (1998). Lamina Properties, Lay-Up Configurations and Loading Conditions for a Range of Fiber-Reinforced Composite Laminates, Composites Science and Technology, 58(7): 1011–1022.

[38] E. Firlar, Examination Of A Micromechanics Based Failure Criterion For Non-Crimp Fiber Reinforced Composite Laminates, MSc Thesis, 2008

[39] H. Myers, D.C.Montgomery, Response Surface Methodology, Wiley Series in Probability and Statistics, 2002

[40] A.Yudhanto, T.E.Tay , Effects Of Micromechanical Factors In The Strain Invariant Failure Theory For Composites, MSc Thesis, 2005

[41] G.Venter, R.T Haftka, Using response surface approximation in fuzzy set based design optimization, Structural Optimization 1, 1-10, 1999

CHAPTER 4

MESO-MACRO

EFFECT OF FIBER YARN COUNT-TEX ON THE STRENGTH AND FAILURE ENVELOPES OF NON-CRIMP GLASS FIBER COMPOSTIES (in cooperation with TELATEKS A.Ş)

4.1 Introduction

Composite materials are progressively replacing metals in aerospace, automotive and marine applications due to their high strength to weight ratio. As promising new materials, the development of those material systems for improved characteristics and performances is of crucial importance for their industrial uses[1]. Elevated in-plane and out-of-plane mechanical response of the composite laminates is at the focus of these developments. As of in-plane properties, very stiff and very strong composite materials may be obtained by the use of unidirectional (UD) reinforcements. They are typically made practical by prepreg technology. However, the manufacturing of pre-preg based composite laminates mostly requires an autoclave process which increases cost substantially. In addition, the storage and use of prepreg materials are limited with their shelf life [2].

Woven fabric reinforcements can lead improved out of plane response and reduced manufacturing costs as their non-prepreg use is also practical. However, their main problem appears to be the crimping of fiber yarns due to the interlacing which significantly reduces the in-plane properties as a result of fiber kinking.

Non crimp fabric (NCF) reinforcement, obtained by stacking layers of unidirectional yarns of different orientations that are stitched together through their thickness, offer fairly good out of plane and in-plane mechanical properties[3-9], as well as low manufacturing costs. Due to their promising properties, the detailed investigation of such materials was carried on by several groups. Lomov et.al for instance published

seven subsequent papers where they investigated the effect of several fabric properties under different loading conditions and made effective computational approximations on the behavior on multi-axial NCF based composite laminates [10-16]. Moreover, Varna [17] and Edgren [18] studied the effects of stitching pattern and the lay-up sequence on the composite properties. In line with the experimental works, several computational studies have investigated the failure and damage mechanisms in NCF composites in order to make effective failure analysis [19-23].

Non-crimp fabric composites have dominant meso-scale architecture where the yarn/matrix interaction is also a factor along with individual fiber/matrix interaction which is typically treated as micro-scale. In meso-scale outlook, yarn number of a NCF composite can also be investigated as an effective factor since for a constant fabric areal weight, it both determines the width of the fiber bundles and the width of the inter-bundle region. From a meso-mechanical point of view these two regions acts as load carriers (bundles) and stress transfer agents (inter-bundle region). This chapter includes the details of a systematic study done for the investigation of the effect of fiber yarn on the strength of non crimp glass fabric (NCGF) reinforced vinyl ester composite laminates.

Four different NCGF TEX as 300, 600, 1200, 2400 were used for custom made of a constant reinforcement ply areal weight and were impregnated by vinyl ester resin system via vacuum assisted resin transfer molding. Laminates with four different lay-up sequences such as $(0)_8$, $(+45/-45)_{4s}$, $(0/90)_{4s}$, and $(0/+45/-45/90)_s$ were studied. Ply strength parameters (X, X', Y, Y', S) and stiffnesses are determined by the tensile and compressive testing of $(0)_8$ and $(+45/-45)_{4s}$ laminates. The failure mechanisms are investigated with respect to changing yarn number. The last ply failure prediction by degradation factor based Tsai-Wu criterion were carried out and failure envelopes for $(0/90)_{4s}$, and $(0/+45/-45/90)_s$ laminates were generated.

4.2. Experimental Procedure and Characterization

4.2.1 Materials

Four different non-crimp fabrics each containing glass fibers of either 300, 600, 1200 or 2400 TEX stitched with synthetic yarn were custom made and provided by Metyx Composites® (Figure 4.1a-4.1d). For all of the fabrics the areal weight was fixed at 300g/m². Fiber bundle size and the distance between the individual fiber bundles were different with increasing yarn number (Table 4.1). All of the dry fabrics were impregnated with Crystic VE-676-03 unsaturated vinyl ester resin supplied by Scott Bader Co. Ltd.

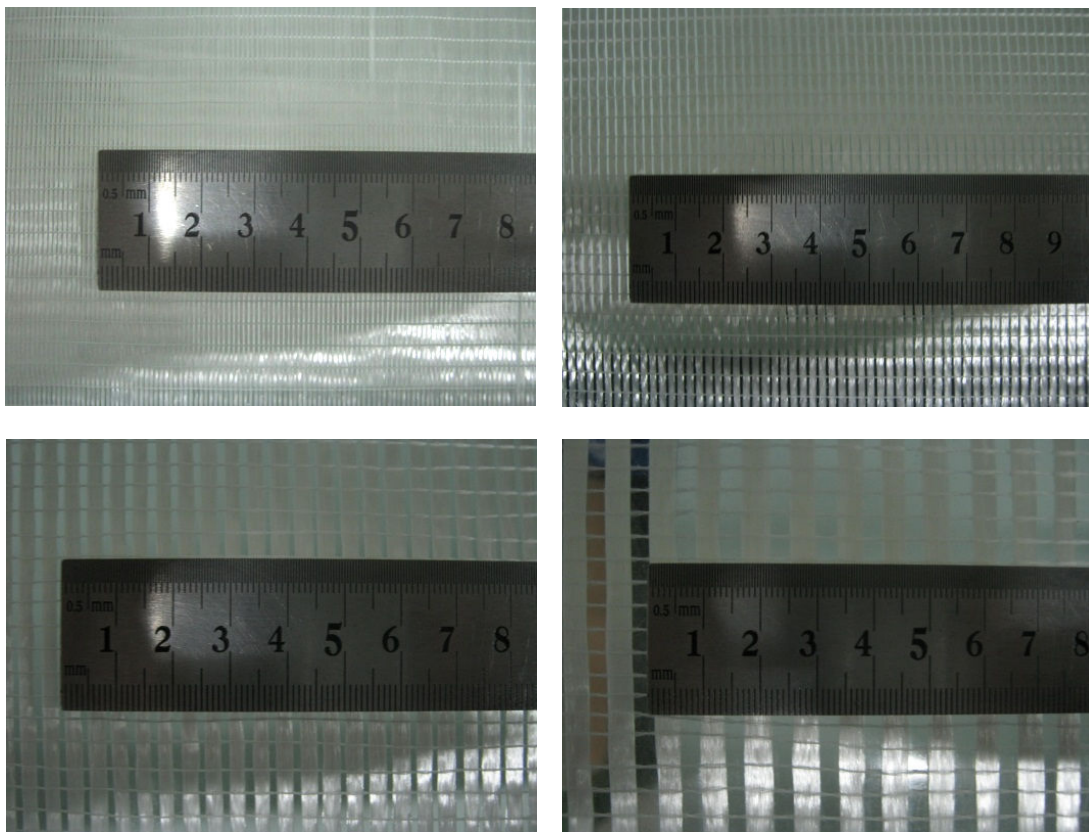


Figure 4.1: a) 300TEX NCGF Fabric b) 600TEX NCGF Fabric c) 1200 TEX NCGF Fabric d) 2400 TEX NCGF Fabric

Table 4.1: Fabric properties for different yarn number

	300 TEX	600 TEX	1200 TEX	2400 TEX
Fiber Diameter (μm)	14	15	16,5	17,5
Bundle Width (μm)	1000	2000	3000	4000
Bundle-Bundle Distance (μm)	500	800	1200	4000

4.2.2 Laminate Manufacturing

Vinyl ester based NCGF composite laminates having 8 layers of dry fabric were manufactured in different lay-up sequences (as in Table 4.2) via vacuum assisted resin transfer molding technique. Vacuum bagging and curing were done at room temperature and under 0,9 bar vacuum pressure (Figure 4.2a-4.2c). Laminates were post cured at 80°C for 3 hours (Figure 4.2d)

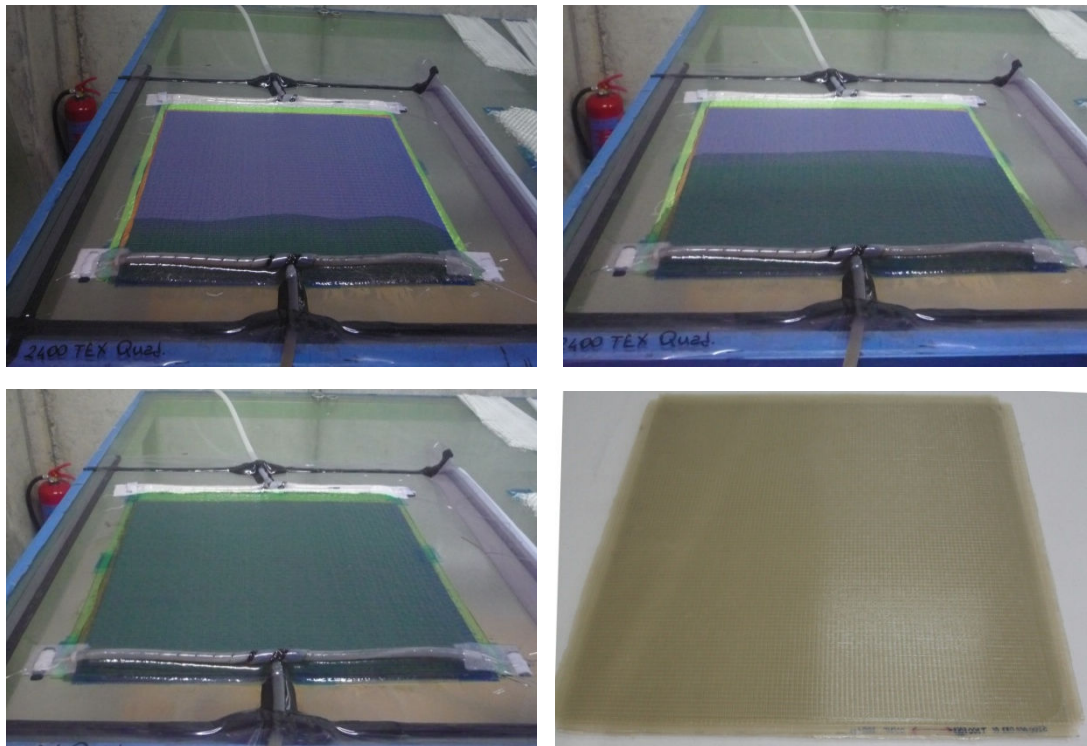


Figure 4.2: a,b,c) Flow front during the vacuum infusion process d) A view from the post-cured laminate ready for specimen cutting.

Table 4.2: Coding of the manufactured laminates according to their lamination sequences

Laminate Coding	300 TEX	600 TEX	1200 TEX	2400 TEX
$(0^\circ)_8$	UD 300	UD 300	UD 1200	UD 2400
$(+45^\circ/-45^\circ)_{4s}$	X 300	X 600	X 1200	X 2400
$(0^\circ / 90^\circ)_{4s}$	LT 300	LT 600	LT 1200	LT 2400
$(0^\circ / +45^\circ / -45^\circ / 90^\circ)_s$	Q 300	Q 600	Q 1200	Q 2400

4.2.3 Mechanical Testing

Tensile tests of cut composite specimens were performed as described in ASTM D3039 test standards. Test specimens were subject to uni-axial tension with a constant displacement rate of 2mm/min and corresponding stress-strain values were recorded for maximum tensile strength and elastic modulus determination both in transverse and longitudinal directions with respect to fiber orientation. Corresponding shear strength and modulus of the laminates were determined out of tensile tests according to ASTM D3518 test standard. A micro-extensometer was used for displacement measurement. ASTM D695 test standard was considered for compression tests. Constant displacement rate was set to 1.3 mm/min. Compressive strength and modulus of the laminates were recorded.

The tensile tests of constituents was also completed where un-reinforced vinyl ester and dry fiber tows were considered

4.2.4 Loss on Ignition Methodology For Fiber Volume Fraction Determination

The determination of the fiber volume fraction is done according to the Loss on Ignition Method as described in ISO1887 test standards. According to this method, first the specimen is placed in a container and its weight is measured (M1). The weight of the container is also measured as C. Then, the specimen is heated up to 120°C in an oven and kept at that temperature for 1 hour for moisture removal and the weight is again measured (M2). Finally, the container is heated to 650°C in the same environment and kept at that temperature for 30 minutes and again its weight is measured (M3). The final fiber weight fraction was determined as $(M3-C)/(M2-C)$. The corresponding fiber volume fraction was calculated by taking the glass fiber density as 2,55 g/cm³ and resin density as 1,2g/cm³.

4.3 Results and Discussion

4.3.1 Fiber Volume Fraction of Laminates

Average fiber volume fractions determined out of the loss on ignition methodology are summarized in table 4.3.

Table 4.3: Fiber volume fractions of manufactured laminates

Fiber Volume Fractions	UD	X	LT	Q
300 TEX	52 %	50 %	52,5 %	52 %
600 TEX	52,5 %	53 %	50 %	51 %
1200 TEX	50 %	52 %	49 %	48 %
2400 TEX	51 %	49 %	48 %	47 %

As it can be seen the average volume fractions of the laminates were close to each other and varied between 47 % and 52 %.

4.3.2 Effect on Longitudinal and Transverse Tensile Strength of Composite Laminates

The failure of (0)₈ laminates was often proceeded by splitting of plies into parallel strips which was mostly initiated from the resin rich inter-bundle regions and caused the final failure of the laminates. Failure of the laminates have occurred after maximum tensile strength was achieved and differentiated by the sudden load drop observed at the end of testing (Figure 4.3a-4.3b). The longitudinal tensile strength of L2400 test coupons was lower due to bigger inter-bundle distance. However, L600 test specimens showed the highest tensile performance rather than the L300 specimens (Table 4.4). The superior behavior of L1200 laminates with respect to L300 and L2400, suggested that the inter-bundle distance could be tuned for better performance rather than choosing the extremes.

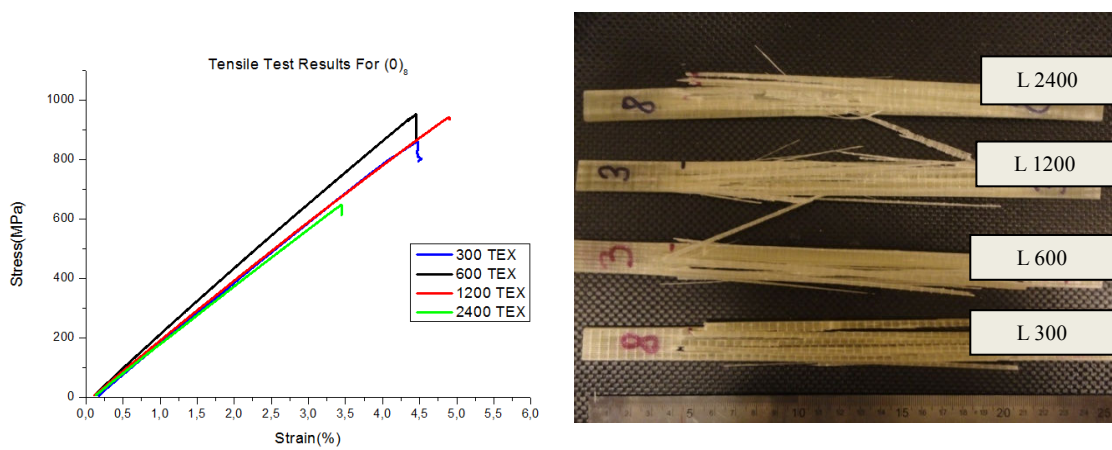


Figure 4.3: a) Representative stress-strain curves for longitudinal tensile testsb)
Ply splitting fracture of (0)₈ laminates

For transversal tensile tests, the observed fracture mode was transverse matrix cracking as expected (Figure 4.4a- 4.4b). Similar to the longitudinal test results, T2400 specimens have shown the lowest performance where as the other specimens have shown close performances. Since the matrix phase is critically loaded under transverse tension loads and the resin system was the same for all test specimens, the difference in the performance outlines the presence of residual stresses that occurred during curing process. As resin rich regions, the inter-bundle spaces were ideal places for the concentration of residual stresses which caused the early matrix cracking for T2400 specimens which could also be a reason for the low longitudinal tensile strength.

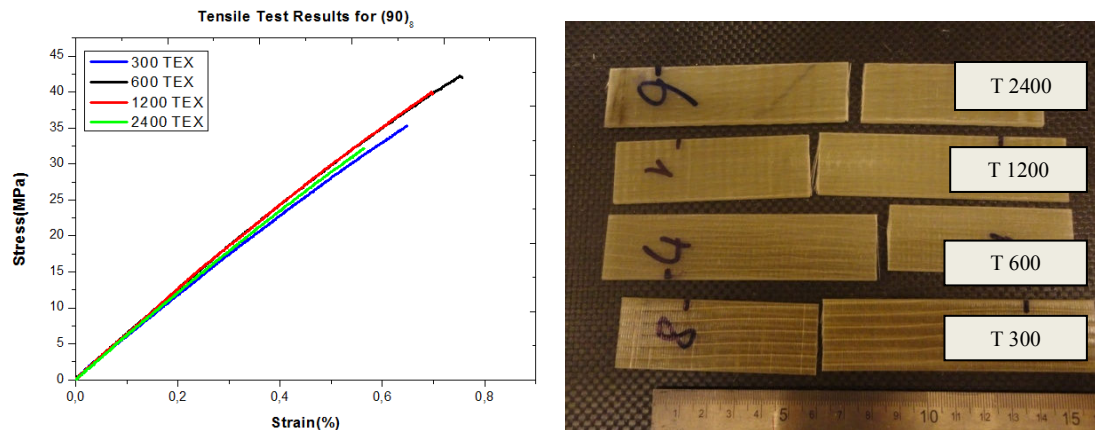


Figure 4.4: a) Representative stress-strain curves for transversal tensile tests
 b) Matrix cracking fracture of $(90)_8$ laminates

Table 4.4: Longitudinal and transverse tensile test results

TEX	Longitudinal Tensile Strength (MPa)	Longitudinal Elastic Modulus (GPa)	Transverse Tensile Strength (MPa)	Transverse Elastic Modulus (GPa)
300	758,1±4,1	38,5±0,4	39,5±0,9	5,4±0.2
600	928,8±12,5	38,8±0,2	42,4±1,9	5,9±0.1
1200	793,8±11,4	39,1±0,5	37,3±1,4	5,8±0.2
2400	654,6±21,5	39,2±0,5	31,8±1,9	5,6±0.3

4.3.3 Effect on the In-Plane Shear Strength of Composite Laminates

The characteristic failure of $[+45/-45]_{4s}$ laminates under uniaxial tension was dominated by a non-linear behavior which was formed of an initial elastic region followed by plastic region. This behavior under shear loading was previously reported on several works in the literature [24-28]. Similar to the works of Van Paepegem the fracture of all the laminates had occurred from the midsection and with an angle of 45° , as a typical shear failure. In the scope of current work, the non-linearity of the stress-strain curves (Figure 4.5a) was observed to be very sensitive to TEX number of the reinforcement. We believe this behavior was due to the tendency of fiber bundles to move in-situ, towards the loading direction. The stress-strain curves in figure 4.5a suggested that the ability to make this movement was related with the yarn number, through the associated bundle width and inter-bundle distance. For instance for X300 laminates, having the smallest bundle width and inter-bundle width, the elastic region was followed by a plastic deformation during which the load increase continued till the necking-like local deformations before failure.

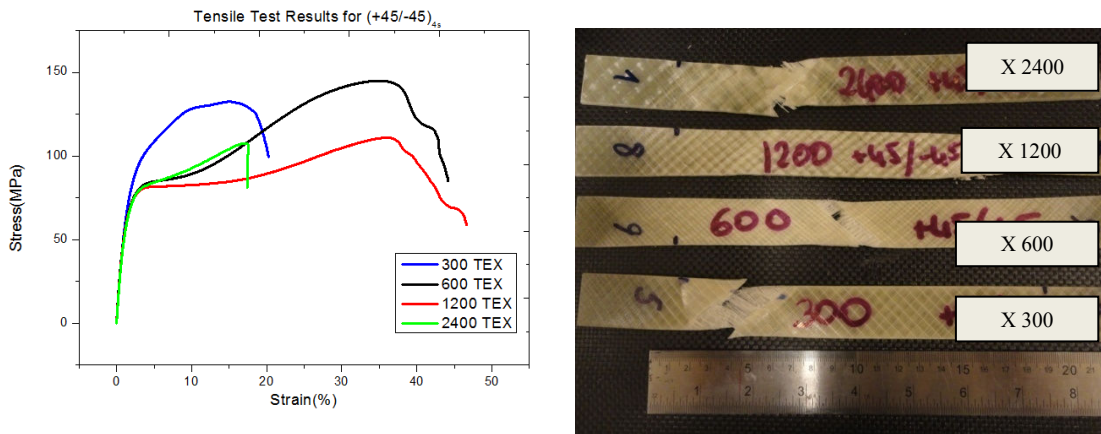


Figure 4.5: a) Representative stress-strain curves for $(+45/-45)_{4s}$ laminates b) Shear mode fracture

On the other hand, the nature of plastic deformation for X600 laminates was somewhat different than X300 laminates where a significant amount of plastic deformation was recorded before the final fracture. Similarly, X600 laminates, X1200

laminates were also able to go through extensive plastic deformation before the fracture. However, different than X600 specimens, X1200 specimens were unable to carry more loads while deforming plastically.. On the contrary, X2400 laminates have again gone through an early failure at the end of a similar plastic behavior seen for X600 and X1200 laminates. The interpretation of this complex behavior requires further experimentation supported with computational methods. However, with these results, we can say that NCGF laminates with small bundle width and inter-bundle distance were able to move more compactly against shear loading. As these widths became larger, the stress transfer between the bundles and equal stress distribution of the fiber bundles has become less efficient (X600, X1200) and after a specific point this compactness totally disappeared which caused an early failure.

Table 4.5: In-plane shear strength and modulus values

Tex	Shear Strength (MPa)	Shear Modulus (GPa)
300	62,9±1.0	6,9±1.0
600	72,4±1,5	6,9±1.5
1200	56,8±1,4	5,4±1.4
2400	42,5±1,8	5,0±1.9

4.3.4 Effect on the Longitudinal and Transversal Compressive Strength

Longitudinal and transversal compression tests of UD laminate were conducted in order to complete all of the ply strength parameters required for the creation of Tsai-Wu failure envelopes. The failure of $(0)_8$ test specimens was initiated by fiber kinking and the ultimate fracture had occurred due to the fiber fracture at the kinking region (Figure 4.6a, 4.6b). Kinking behavior was differentiated by the deformation pattern during testing (Figure 4.6c). The transversal direction the fracture occurred due to the matrix cracking.

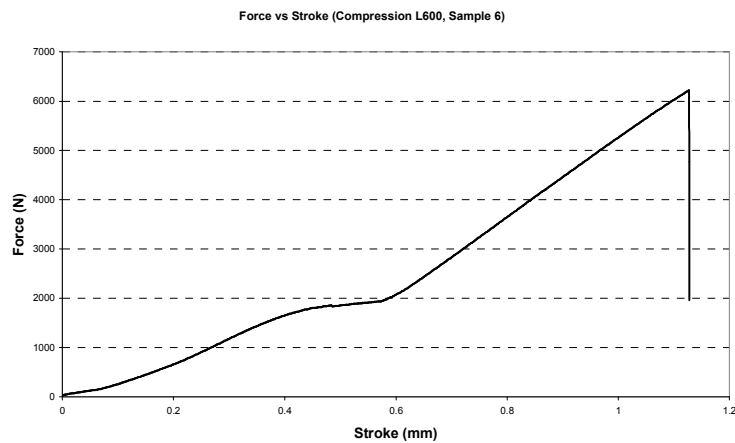
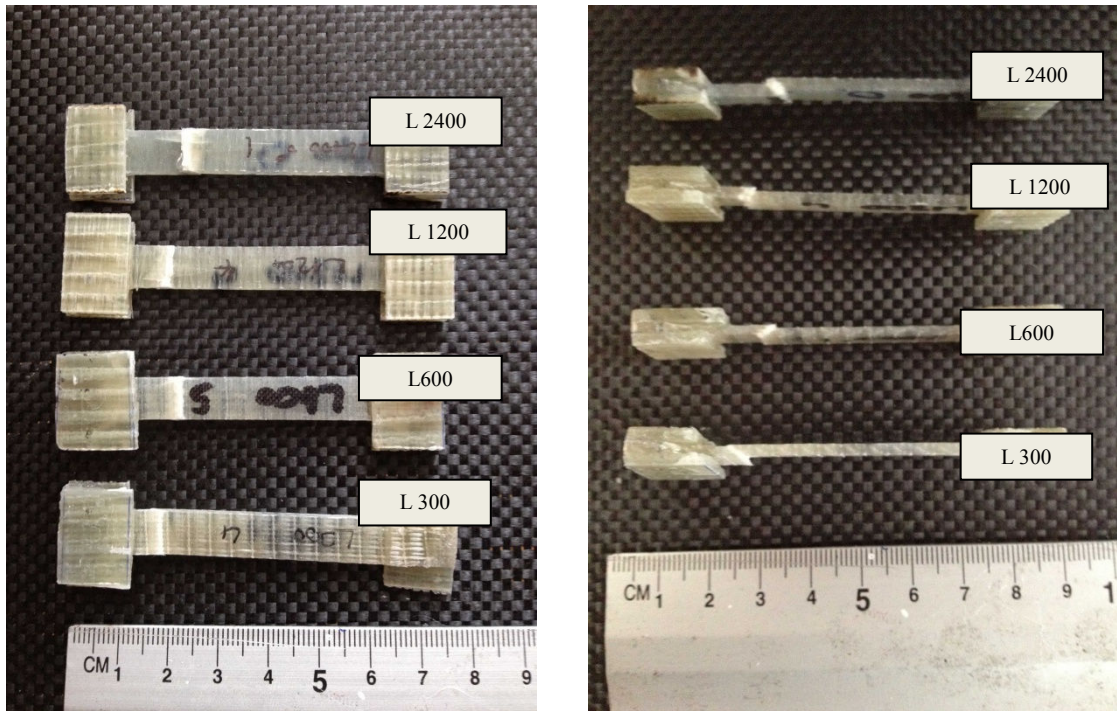


Figure 4.6. Compression tests a) Fractured $(0)_8$ laminates b) Side-view of fractured $(0)_8$ laminates

Different from the tensile test results, for longitudinal compression tests, the performance of each laminate was very close. The reason for the consistency, may be the fact that the fracture was dominated by fiber failure. However the exact reason is still under investigation. Finally, the transversal compression test results were also very close to each other.

Table 4.6: Longitudinal and transversal compressive strength and modulus values

TEX	Longitudinal Compressive Strength (MPa)	Longitudinal Compression Modulus (GPa)	Transversal Compressive Strength (MPa)	Transversal Compression Modulus (GPa)
300	285,0±10,4	24,5±1,7	128,4±1,5	10,1±0,1
600	318,8±23,1	24,2±1,6	131,9±0,8	10,5±0,1
1200	301,1±21,1	23,2±1,4	126,2±3	9,4±0,2
2400	329,7±16,5	26,4±1,7	123,4±2	9,3±0,2

4.3.5 Tsai-Wu Based Failure Envelopes and Correction Cases

The ply strength parameters (X , X' , Y , Y' 'S) and stiffness parameters that were extracted out from the above mentioned tensile and compressive tests. These parameters were used in the creation of Tsai-Wu failure envelope as anchor points. The capability of Tsai-Wu failure criteria to predict the last ply failure of each laminate with different yarn numbers was sought through the comparison of test results obtained from the tensile tests of a cross-ply $(0/90)_{4s}$ laminate and a quasi-isotropic $(0/+45/-45/90)_s$ laminate.

For the prediction of last ply failures, a property degradation based methodology offered by MicMac [29] software was used. For a brief information, this methodology assumes that once the first ply failure is achieved, the properties of one or more plies become simultaneously degraded due to the formation of micro cracks or catastrophic fiber break or buckling. For our case, the matrix degradation factor was fixed to 0.2 and the fiber degradation factor was fixed to 0.01. In addition to that the interaction term F_{xy} was set at -0.5. The details of these parameters and how they are implemented to the failure analysis may be found in reference [29] in detail. According to this the last failure envelopes of tested correction case laminates on σ_1 - σ_2 stress plane and corresponding test date were found as in figures 4.8-4.10.

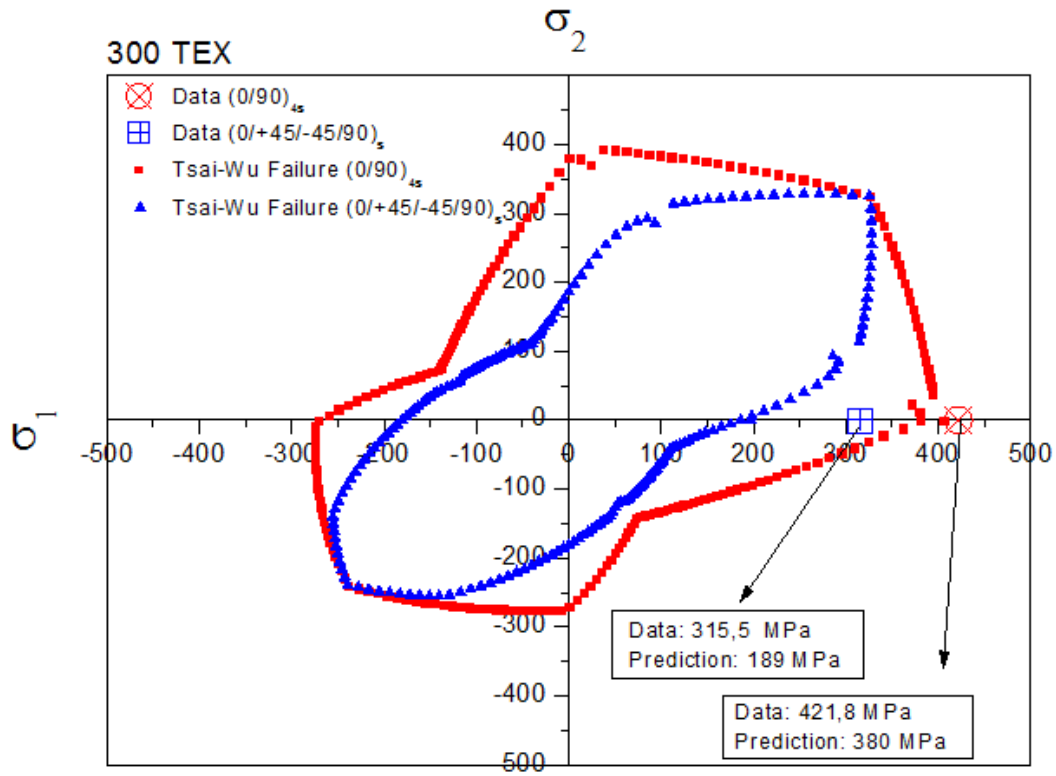


Figure 4.7: Tsai-Wu Failure envelopes for (0/90)_{4s} and (0/+45/-45/90)_s laminates with 300 TEX NCGF reinforcement

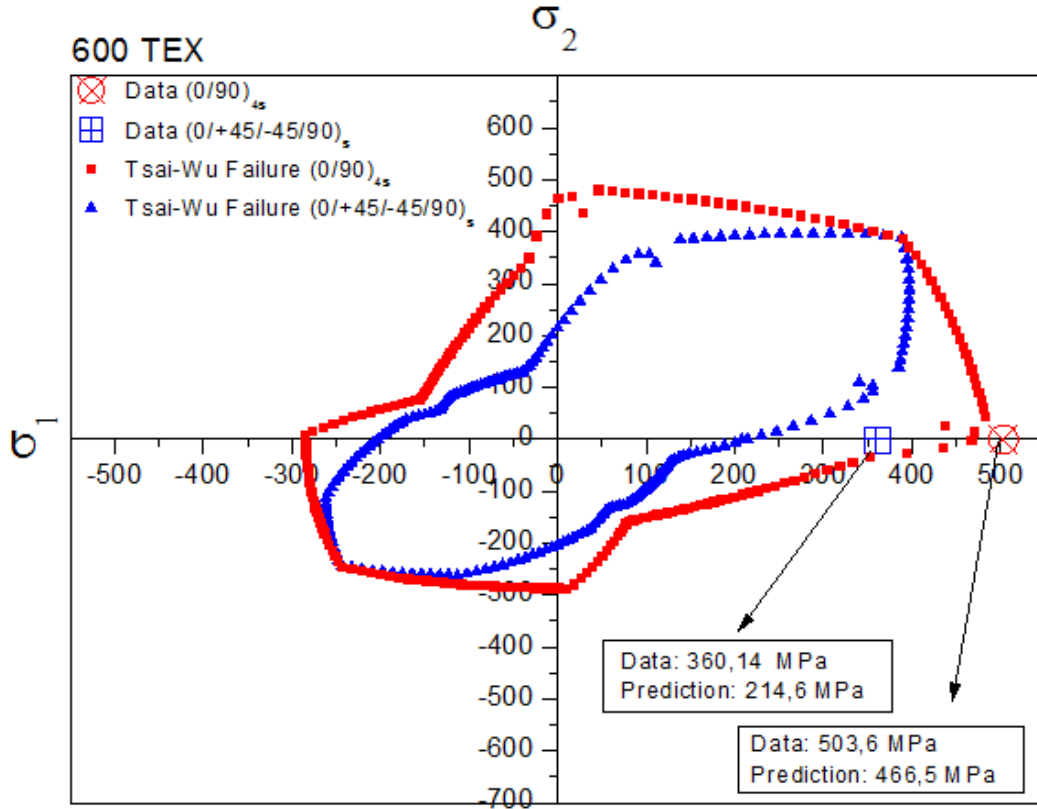


Figure 4.8: Tsai-Wu Failure envelopes for (0/90)_{4s} and (0/+45/-45/90)_s laminates with 600 TEX NCGF reinforcement

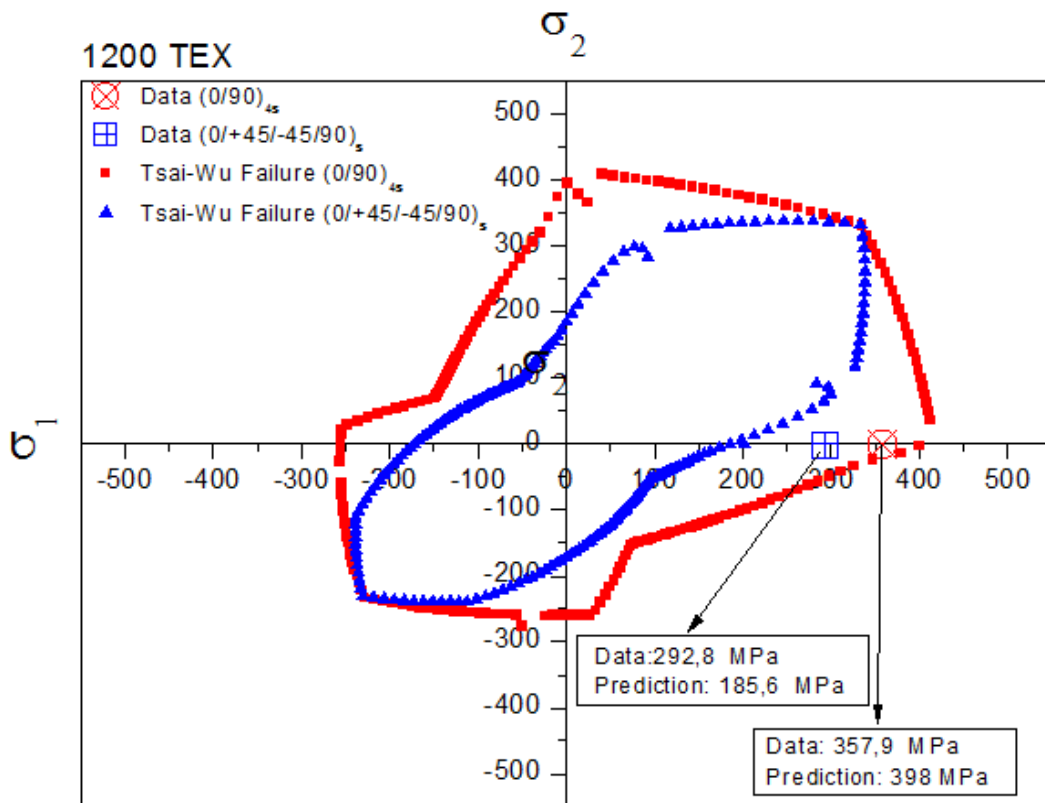


Figure 4.9: Tsai-Wu Failure envelopes for $(0/90)_{4s}$ and $(0/+45/-45/90)_s$ laminates with 2400 TEX NCGF reinforcement

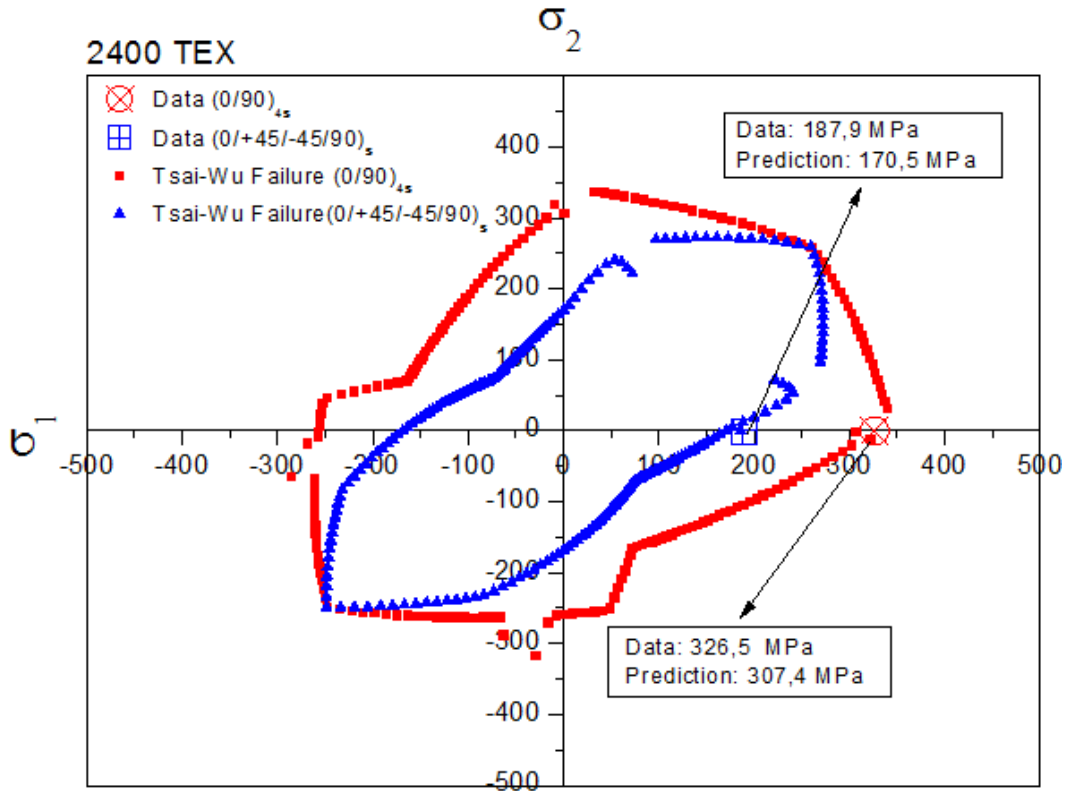


Figure 4.10: Tsai-Wu Failure envelopes for $(0/90)_{4s}$ and $(0/+45/-45/90)_s$ laminates with 1200 TEX NCGF reinforcement

The results suggested that the predictions done with Tsai-Wu failure criteria were in a reasonable error range for $(0/90)_{4s}$ laminates. Whereas for $(0/+45/-45/90)_s$ laminates Tsai-Wu failure was not able give good predictions. One reason for that inability may be the complex failure mechanism observed for +45 and -45 plies since Tsai-Wu failure criteria is not very sensitive to the plastic deformation occurring in the testing of such plies.

Table4.7: Test Results for $(0/90)_{4s}$ and $(0/+45/-45/90)_s$ laminates and predicted Tsai-Wu failure strengths

Tex	$(0/90)_{4s}$ Strength (MPa)	Tsai-Wu Failure Prediction $(0/90)_{4s}$ (MPa)	Difference (%)	$(0/+45/-45/90)_s$ Strength (MPa)	Tsai-Wu Failure Prediction $(0/+45/-45/90)_s$ (MPa)	Difference (%)
300	421,8	380	-9,9	315,5	189	-40,1
600	503,6	466,5	-7,4	360,1	214,6	-40,4
1200	357,9	398	11,2	292,8	185,6	-36,6
2400	326,5	307,4	-5,8	187,9	170,5	-9,3

4.3.6 Micromechanics Based Back-Calculation of Constituent Properties

A simple micromechanical failure analysis was also conducted for UD laminates where the strength of constituents, namely fiber tows and resin , were back calculated by using the micromechanics of failure theory as explained in chapter 3. Basically, the micromechanics based stress amplification factors were used as amplifiers to the macro stresses determined by the lamina testing, in order to calculate the constituent strength according to maximum stress failure criterion. Stress amplifications for both Square and Hex and RVEs were calculated through the use of SMM+ software [29]. The strength of fibers was determined through the tensile tests of fiber tows. Due to complexity of the testing associated with the gripping properly, it was very hard to determine the elastic modulus of fiber tows. Hence, the longitudinal fiber modulus used as inputs in the micromechanics based RVEs were determined by a simple rule of mixture based on

UD laminate testing and fiber volume fractions. Determined constituent strengths and stiffnesses are summarized in table 4.8 where as the corresponding stress amplification factors can be found in table 4.9.

Table 4.8: Constituent properties for micromechanical analysis

TEX	Fiber Diameter (μm)	Fiber Volume Fraction (%)	Fiber Longitudinal Elastic Modulus (GPa)	Resin Elastic Modulus (GPa)	Fiber Strength (MPa)	Resin Strength (MPa)
300	14	52 %	77	3,44	2826	49,8
600	15	52,5 %	77,6	3,44	2801,3	49,8
1200	16,5	50 %	78,2	3,44	3087.0	49,8
2400	17,5	51 %	78,4	3,44	2486,8	49,8

Table 4.9: MMF based stress amplification factors for matrix and fiber phases

Model Type	Critical Fiber Amplification Factors (300-600-1200-2400)	Critical Resin Amplification Factors (300-600-1200-2400)
Square	1,85-1,84-1,92-1,89	1,17-1,17-1,18-1,18
Hex	1,85-1,83-1,91-1,88	1,17-1,18-1,18-1,18

The predicted constituent properties are summarized in tables 4.10-4.11

Table 4.10: Back calculated fiber strengths for different micromechanical models

TEX	(0) ₈ Strength (MPa)	Predicted Fiber Strength by Sqr RVE	Predicted Fiber Strength by Hex RVE	Actual Fiber Strength (MPa)
300	758,1	1402,4	1402,4	2826
600	928,8	1708,9	1700	2801,3
1200	793,8	1524,1	1532,1	3087,0
2400	654,6	1236,8	1230,4	2486,8

Table 4.11: Back calculated resin strengths for different micromechanical models

TEX	(90) ₈ Strength (MPa)	Predicted Resin Strength by Sqr RVE	Predicted Resin Strength by Hex RVE	Actual Resin Strength (MPa)
300	39,5	46,2	46,2	49,8
600	42,4	49,6	50,1	49,8
1200	37,3	44,1	44,1	49,8
2400	31,8	37,5	37,5	49,8

As it can be deduced from the predictions, using MMF criteria was not efficient in terms of predicting the micro stresses that has caused the final failure. Most important reason of this observation was, in support with the previous observations about matrix cracking and effect of inter-bundle distance, that MMF assumes that the ultimate fracture of a UD specimens is dominated by fiber fracture and the fiber fracture occurs when the

ultimate tensile strength of fibers were reached. However, for the problem in hand, the failure of UD specimens was dominated by critical matrix cracking. That is why, there were significant differences between the ultimate tensile strength of test specimens with different yarn numbers, although the fiber strengths and volume fractions were close to each other.

On the other hand, the back calculation of resin strength out of transversal tensile tests can be considered as successful by using MMF. Although both hexagonal and square array models were able to give good predictions for T300, T600 and T1200 laminates they were unable to predict the resin strength of T2400 laminates. This inability once again signifies the presence of unwanted residual stresses in the inter-bundle regions which are not taken into consideration in the present MMF analysis and the lack of meso-scale introduction to the failure modeling.

4.4 Conclusions and Future Works

The conclusions and the achievements to be underlined as a result of the content of this chapter may be counted as follows:

- Non-crimp glass fabric composite laminates having different fiber yarn numbers and constant areal weight were manufactured successfully by vacuum assisted resin transfer molding process. Obtained laminates had reasonable and close fiber volume fractions.
- The effect of yarn number, hence the fiber bundle width and inter-bundle distance, on the mechanical response of the laminates was studied.
- It was observed that the yarn number has a significant effect under longitudinal tensile and in-plane shear load condition whereas minor effects under other loadings considered such as longitudinal and transversal compression. For the longitudinal tension tests, it was shown that the inter-bundle distance had to be tuned for better mechanical performances rather than choosing it on the extremes as in the cases of L300 and L2400 laminates where the mechanical performance was lower.
- For in-plane shear tests, again a significant difference was observed with changing yarn counts, TEX numbers. For this test case, the movement of fiber bundles towards the loading direction was again controlled by inter-bundle region as the loading and deformation proceed. Compactness and separated nature of the fabrics have directly shown itself in the test results as different plastic responses.
- Tsai-Wu ply strength parameters extracted out of mechanical test results and were used in the creation of ply degradation based last ply failure analysis of laminates $(0/90)_{4s}$ and $(0/+45/-45/90)_s$.
- With Tsai-Wu failure analysis based on the macro level stresses, the tensile strength of $(0/90)_{4s}$ laminates was predicted accurately. However, it was unable to predict the tensile strength of $(0/+45/-45/90)_s$ laminates. This inability is

attributed to the complex behavior of +45 and -45 plies under tensile loadings which is not taken into account in the Tsai-Wu failure analysis.

- The ability of Micromechanics of failure to predict this effect was tested with simple back calculation of constituent properties out of tensile testing of UD laminates via stress amplification factors extracted out of square, hexagonal and octagonal array representative volume elements.
- Resin strength was predicted efficiently with MMF except for T2400 laminates where the residual stresses were present.

As an overall view, throughout this chapter conventional steps were followed for a standard failure exercise. Systematic investigation of the effect of yarn number was done with a systematic manufacturing and testing process.

The general plot suggested that none of the most conventional failure criteria either based on macro stresses or micro stresses was able to give perfect predictions on the effect of yarn number on the strength of NCGF laminates. Having investigated that systematically, the outputs of this chapter will be used in the creation of meso-scale models whose prediction capabilities will be compared with the ones of MMF and Tsai-Wu failure criteria. Also the test database will be extended with the compression and open hole tension tests of $(0/90)_{4s}$ and $(0/+45/-45/90)_s$ laminates which will be used as correction data points as well.

4.5 References

- [1] K.I. Tserpes, G.N. Labeas "Mesomechanical analysis of non-crimp fabric composite structural parts" *Composite Structures*, 87(4):358-69, 2009
- [2] D. Mattsson, R. Joffe, J.Varna "Methodology for characterization of internal structure parameters governing performance in NCF composites", *Composites Part B: Engineering*, 38(1):44-57, 2007
- [3] K. Dransfield, C. Baillie, Y-W.Mai "Improving the delamination resistance of CFRP by stitching-a review." *Compos Sci Technol*, 50:305–17, 1994
- [4] K. Dransfield, L. Jain L, Y-W Mai, "On the effects of stitching in CFRPsI. Mode I delamination toughness.", *Compos Sci Technol*, 58: 815–27, 1998
- [5] L. Jain L, K. Dransfield, Y-W. Mai. "On the effects of stitching in CFRPsII. Mode II Delamination toughness. *Compos Sci Technol*, 58:815–27, 1998
- [6] F. Edgren, D. Mattsson, L.E. Asp, J. Varn, Formation of damage and its effects on non-crimp fabric reinforced composites loaded in tension, *Compos Sci Technol*, Vol.64, pp. 675–692 (2004)
- [7] K.Vallons, S.V. Lomov, I.Verpoest, Fatigue and Post Fatigue behaviour of carbon/epoxy non-crimp fabric composites, *Composites Part A: Applied Science and Manufacturing*, Vol.40, pp. 251-259, (2009)
- [8] F.L. Edgren, E. Asp, R. Joffe Failure of NCF composites subjected to combined compression and shear loadings, *Compos Sci Technol*, Vol. 66, pp. 2865–2877 (2006)

- [9] K. Vallons, A. Behaeghe, S. V. Lomov, I. Verpoest, Impact and post-impact properties of a carbon fibre non-crimp fabric and a twill weave composite, *Composites Part A: Applied Science and Manufacturing*, Vol. 41, pp. 1019-1026, (2010)
- [10] Lomov SV, Belov EB, Bischoff T, Ghosh SB, Chi TT, Verpoest I. Carbon composites based on multiaxial multiply stitched preforms. Part 1. Geometry of the preform. *Composites Part A* 2002;33(9):1171–83.
- [11] Lomov SV, Verpoest I, Barburski M, Laperre J. Carbon composites based on multiaxial multiply stitched preforms. Part 2. KES-F characterisation of the deformability of the preforms at low loads. *Composites Part A* 2003;34(4):359–70
- [12] Lomov SV, Barburski M, Stoilova T, Verpoest I, Akkerman R, Loendersloot R, et al. Carbon composites based on multiaxial multiply stitched preforms. Part 3: biaxial tension, picture frame and compression tests of the preforms. *Composites Part A* 2005;36(9):1188–206.
- [13] Truong TC, Vettori M, Lomov S, Verpoest I. Carbon composites based on multiaxial multi-ply stitched preforms. Part 4. Mechanical properties of composites and damage observation. *Composites Part A* 2005;36(9):1207–21.
- [14] Loendersloot R, Lomov SV, Akkerman R, Verpoest I. Carbon composites based on multiaxial multiply stitched preforms. Part V: geometry of sheared biaxial fabrics. *Composites Part A* 2006;37(1):103–13.
- [15] Vallons K, Zong M, Lomov SV, Verpoest I. Carbon composites based on multiaxial multi-ply stitched preforms – Part 6. Fatigue behaviour at low loads: stiffness degradation and damage development. *Composites Part A* 2007;38(7):1633–45
- [16] Truong TC, Ivanov DS, Klimshin DV, Lomov SV, Verpoest I. Carbon composites based on multi-axial multi-ply stitched preforms. Part 7: mechanical properties and damage observations in composites with sheared reinforcement. *ComposPart A: Appl Sci Manuf* 2008;39(9):1380–93.

- [17] D.Mattsson, R.Joffe, J. Varna, Damage in NCF composites under tension: Effect of layer stacking sequence, *Engineering Fracture Mechanics*, vol. 77:2666-268 (2008)
- [18] Edgren FL, Asp E, Sjögren A. Effects of stitch pattern on the mechanical properties of non-crimp fabric composites. In: ECCM 11. Rhodos; 2008.
- [19] S. Drapier, M.R. Wisnom Finite-element investigation of the compressive strength of non-crimp-fabric-based composites, *Compos Sci Technol*, Vol.59 ,pp. 1287–1297 (1999)
- [20] S. Drapier, M.R. Wisnom A finite-element investigation of the interlaminar shear behaviour of non-crimp-fabric-based composites, *Compos Sci Technol*, Vol. 59 pp. 2351–2362, (1999)
- [21] A. Gonzalez, E.Graciani, F.Paris, Prediction of in-plane stiffness of non-crimp fabric laminates by means of 3D finite element analysis, *Compos Sci Technol*, Vol.6pp.121-131, (2008)
- [22] H. Heß, N. Himmel, Structurally stitched NCF CFRP laminates. Part 2: Finite element unitcell based prediction of in-plane strength, *Composites Science and Technology*, Vol.71, pp.569-585, 2011
- [23] L.G. Zhao, N.A. Warrior, A.C. Long, Finite element modelling of damage progression in non-crimp fabric reinforced composites, *Composites Science and Technology*, Vol. 66, pp.3650, 2006
- [24] H.T Hahn, S.W Tsai, Non-Linear Elastic Behaviour of Unidirectional Composite Laminate, *Journal of Composite Materials*, Vol. 7, pp. 102-118, (1973)
- [25] W.P. Lin, H-T Hu. , Nonlinear Analysis of Fiber-Reinforced Composite Laminates Subjected to Uniaxial Tensile Load, *Journal of Composite Materials*, Vol.36 pp.1429-1450,(2002)

- [26] J. Cho, J. Fenner, B. Werner, I.M. Daniel, A Constitutive Model for Fiber-reinforced Polymer Composites, *Journal of Composite Materials* 2010 Vol. 44, pp. 3133-315
- [27] Van Paepegem, W., De Baere, I. and Degrieck, J.. Modelling the non-linear shear stress-strain response of glass fibre reinforced composites. Part I: Experimental results. *Composites Science and Technology*, Vol.66, pp.1455-1464, (2006)
- [28] Van Paepegem, W., De Baere, I. and Degrieck, J. (2006). Modelling the nonlinear shear stress-strain response of glass fibre-reinforced composites. Part II: Model development and finite element simulations. *Composites Science and Technology* , Vol. 66, pp.1465-1478.
- [29] S.W.Tsai, Strength and Life of Composites, JEC Composites, 2008